Meteoritics & Planetary Science 1–19 (2023)
doi: 10.1111/maps.13957

Petrology and mineralogy of mesosiderite Northwest Africa 12949: Implications for geological history on its parent body

Zilong WANG[1,2] and Wei TIAN[1]*

[1]The Key Laboratory of Orogenic Belts and Crustal Evolution, Ministry of Education, School of Earth and Space Sciences, Peking University, Beijing, China
[2]The Key Laboratory of Paleomagnetism and Tectonic Reconstruction of MNR, Institute of Geomechanics, Chinese Academy of Geological Sciences, Beijing, China
*Corresponding author.
Wei Tian, Key Laboratory of Orogenic Belts and Crustal Evolution, Ministry of Education, School of Earth and Space Sciences, Peking University, Beijing 100871, China.
E-mail: davidtian@pku.edu.cn

(Received 06 April 2022; revision accepted 18 January 2023)

Abstract–Mesosiderites are breccias composed of roughly equal parts of metal phases and silicate clasts. However, the parent body and formation process of mesosiderites remain enigmatic. Northwest Africa (NWA) 12949 is a newly found mesosiderite belonging to type 2A. One type of ultramafic clasts and four types of mafic clasts (gabbroic, poikilitic, subophitic, and cataclastic), compositionally consistent with diogenites and eucrites, have been identified in NWA 12949. However, these clasts have undergone different thermal histories, with cooling rates varying from ~0.0044 °C year^{-1} to a few °C h^{-1}, and equilibrium temperatures varying from ~880 to 910 °C to ~1000 to 1100 °C. All the lithic clasts have undergone redox reactions during extensive metamorphism, forming excess troilite, chromite, merrillite, tridymite, and pyroxene with lower Fe/Mg and Fe/Mn. The petrology and mineralogy of NWA 12949 support a formation scenario involving two major impact events, and a candidate parent body of 4 Vesta.

INTRODUCTION

Mesosiderites are breccias composed of roughly equal parts of metal phases and silicate clasts in a fragmental igneous groundmass (Floran, 1978; Powell, 1971). The silicate phases consist of lithic and mineral clasts embedded in groundmass (Krot et al., 2014). The lithic clasts are largely basalts, gabbros, and pyroxenites, while dunites and anorthosites are rare (Mittlefehldt, 2014). The mineral clasts include pyroxene, olivine, and plagioclase (Hewins, 1984; Krot et al., 2014). The metal fraction of mesosiderites mainly consists of IIIAB-like kamacite, taenite, and troilite (Hassanzadeh et al., 1990; Wasson et al., 1974, 1998). All the mesosiderites have a nearly identical formation age, with the silicate clasts forming at 4558.5 ± 2.1 Ma and metal–silicate mixture forming at 4525.39 ± 0.85 Ma (Haba et al., 2019).

In general, the origin of mesosiderites remains an open question. Previous studies have proposed that mesosiderite silicates are genetically related to the howardite, eucrite, and diogenite (HED) meteorite clan, due to strong similarities between their mineralogy, textures, bulk compositions, formation ages, and oxygen isotopic studies (Bogard & Garrison, 2003; Floran, 1978; Greenwood et al., 2006, 2015; Kennedy et al., 2019; Mittlefehldt et al., 1998; Powell, 1971; Rubin & Jerde, 1987; Rubin & Mittlefehldt, 1993). The HEDs are the largest group of crustal igneous meteorites and are believed to have originated on asteroid 4 Vesta (e.g., Binzel & Xu, 1993; Consolmagno & Drake, 1977; McCord et al., 1970; McSween et al., 2013). Hence, a common origin of the mesosiderites and the HEDs from the asteroid 4 Vesta has been proposed (Haba et al., 2019; Sugiura et al., 2022). However, there are fundamental differences between the compositions of HEDs and mesosiderite silicates, such as the pyroxene Fe-Mn-Mg systematics (Delaney et al., 1981; Lelarge et al., 2022; Mittlefehldt, 1990; Mittlefehldt et al., 2021), and the modal abundances of silicates, phosphates, and chromite (Mittlefehldt, 2014; Mittlefehldt et al., 1998). Some clasts of mesosiderites also show more complex rare-earth-element patterns (Mittlefehldt et al., 1998; Rubin & Mittlefehldt, 1993). Besides, the spectral evidence indicates that the surface of Vesta is metal-poor, inconsistent with the metal-rich lithology of mesosiderites (McSween & Binzel, 2022; Mittlefehldt et al., 2012; Prettyman et al., 2012). Alternatively, the metal-rich asteroid 16 Psyche (Viikinkoski et al., 2018) or the Xk-type asteroids (Vernazza et al., 2009) may be the potential parent body of mesosiderites.

Mesosiderites have experienced complicated thermal histories. The well-accepted formation model of mesosiderites (e.g., Rubin, 1997; Rubin & Mittlefehldt, 1993; Scott et al., 2001) can be divided into the following stages: (1) accretion and initial crystallization of mesosiderite silicates at 4.56–4.47 Ga (Haba et al., 2019; Stewart et al., 1994; Wadhwa et al., 2003); (2) collisional disruption and intense brecciation (Haba et al., 2017; Jourdan et al., 2021); (3) mixing of metal and silicates and rapid cooling (Delaney et al., 1981; Ganguly et al., 1994; Ruzicka et al., 1994; Tamaki et al., 2006); (4) deep burial and slow cooling (Bogard & Garrison, 1998; Haack et al., 1996; Hopfe & Goldstein, 2001; Yang et al., 1997); and (5) impact excavation and ejection at <4 Ga (Bogard, 2011; Bogard et al., 1990; Kring & Cohen, 2002). However, several key processes of mesosiderite formation have remained unclear, including the number of impact and reheating events, the time of metal and crustal silicate mixing, the degree and the peak temperatures of thermal metamorphism, and the emplacement depths in each thermal event (e.g., Caves, 2019; Pittarello et al., 2019; Sugiura et al., 2022).

Northwest Africa (NWA) 12949 is a newly found mesosiderite that has not been studied and reported before. This sample is a polymict breccia containing various clasts with different emplacement environments and thermal histories. In this study, we first report the textures and mineral compositions of the lithic clasts in NWA 12949. Then, we calculate cooling rates and burial depths and determine the metamorphic reactions of these clasts. These results allow us to reconstruct the thermal history of mesosiderite NWA 12949. This study will add to the understandings of the relationship between mesosiderites and HEDs and the geological history of the mesosiderite parent body.

SAMPLE AND ANALYTICAL METHODS

Found in Morocco in 2019, NWA 12949 is one of 316 mesosiderites (by Feburary 7, 2023) so far found. Both the shock stage and weathering grade of NWA 12949 are low (see Meteoritical Bulletin Database). In this study, a slice of NWA 12949 rock weighing 5.4 g was obtained from Fabien Kunz in June 2021. The sample is fresh, with no fusion crust and minor terrestrial contamination, showing that it is from the interior of the meteorite and thus preserves primitive features. The slice was polished into a thin section for the research.

TESCAN Integrated Mineral Analyzer Analyses

A polished thin section of NWA 12949 was analyzed using the TESCAN Integrated Mineral Analyzer (TIMA) mineralogy system (Hrstka et al., 2018) at the Key Laboratory of Orogenic Belts and Crustal Evolution, School of Earth and Space Sciences, Peking University, China. The TIMA comprises a Tescan Mira Schottky field emission automated scanning electron microscopy system with four silicon drift energy dispersive spectroscopy detectors arranged around the chamber at approximately 90° intervals. The measurements were performed in high-resolution liberation analysis mode. Backscattered electron (BSE) images were acquired to define individual particles and the boundaries between distinct phases. A rectangular mesh of X-ray spectral measurements was obtained for each particular phase. TIMA analyses were conducted at a working voltage of 25 kV with a spot size of 1 μm, a working distance of 15 mm, and a field size of 1000 μm studying all zones in the thin section. At each pixel, an energy dispersive X-ray spectrum was rapidly acquired and, along with the BSE signal, used to determine elemental X-ray maps (Al, Ca, Fe, Mn, Mg, Si, P, S, Ti, and Ni).

Mineral Chemistry by Electron Probe Microanalysis

Quantitative chemical analyses of minerals in the polished thin section NWA 12949 were conducted using a JEOL JXA-8230 electron probe microanalyzer (EPMA) equipped with four wavelength dispersive spectrometers at the Key Laboratory of Orogenic Belts and Crustal Evolution of School of Earth and Space Sciences, Peking University. The acceleration voltage and the beam current were 15 kV and 10 nA, respectively. The beam diameter was set to “spot” mode (minimum instrument size) or 1–2 μm, and a counting time of 20 s was used for both peak and background. The SPI 53 minerals standard (U.S.) was utilized for the quantitative analysis: sanidine was employed for K; diopside for Ca and Mg; rutile for Ti; jadeite for Na, Al, and Si; chromium oxide for Cr; rhodonite for Mn; hematite for Fe; and nickel silicide for Ni. At the final calibration stage, the PRZ correction was performed (Pouchou & Pichoir, 1985). Detection limits of the oxides were 0.01 wt% for K_2O; 0.02 wt% for Al_2O_3 and Na_2O; 0.03 wt% for MgO and CaO; 0.04 wt% for TiO_2, Cr_2O_3, MnO, FeO, and NiO; and 0.06 wt% for SiO_2.

Raman Spectrometry

Raman spectra of the silica in the sample were collected using a LabRAM HR Evolution (HORIBA Jobin Yvon) spectrometer system at Peking University, equipped with a frequency-doubled Nd:YAG laser (at 532 nm). Each Raman spectrum was acquired between 100 and 1800 cm^{-1} with a spectral resolution of 0.7 cm^{-1} and an acquisition time of 20–30 s. All spectra were processed by PeakFit software (SeaSolve Software Inc.) and were calibrated against the measured excitation of Si at ~520 cm^{-1}. After the baseline was subtracted with a reasonable function, the Raman peaks were fitted using the symmetric Gauss + Lorentz function.

Bulk Composition Reconstruction for Clasts

We constructed a mineral distribution map using a modified method developed by Hahn et al. (2017) and references therein to determine modal abundances and locate mineral grains of interest. Specifically, we used a combination of elemental X-ray maps collected by TIMA; this combination of elements provides adequate compositional resolution. After data collection, the elemental maps were combined into a geochemical information cube, analogous to a multispectral image cube, using ENVI 5.3. Phases with known mineral compositions, determined from point analyses, were used to define regions of interest (ROIs) for each phase present in the assemblage. A minimum distance classification was then applied, where all pixels in the image are assigned to a class according to their distance from the ROI mean. Pixels that lie outside the standard deviation set for each class are deemed unclassified. Before classification, we used a minimum value protocol to mask out cracks and the surrounding background to create a more accurate modal classification. Classification trials were run, and ROIs were adjusted until the unclassified pixels were less than 10%.

To reconstruct the bulk composition of the lithic clasts in NWA 12949, we combined EPMA average mineral analyses with modal abundances determined from the mineral maps. The bulk composition was determined using Equation (1), which incorporates the phase density, and allows for more accurate bulk compositions (Hahn et al., 2017). The bulk compositions of the clasts were calculated using all mineral phases in the assemblage.

$$\begin{aligned}\text{Elem.A} = {} & C_{\text{Ph.1}}^{\text{Elem.A}} \times \left[\frac{\text{Vol\%}_{\text{Ph.1}} \times \rho_{\text{Ph.1}}}{\sum_1^n (\text{Vol\%}_{\text{Ph.}} \times \rho_{\text{Ph.}})}\right] \\ & + C_{\text{Ph.2}}^{\text{Elem.A}} \times \left[\frac{\text{Vol.\%}_{\text{Ph.2}} \times \rho_{\text{Ph.2}}}{\sum_1^n (\text{Vol\%}_{\text{Ph.}} \times \rho_{\text{Ph.}})}\right] \\ & + \cdots + C_{\text{Ph.}n}^{\text{Elem.A}} \times \left[\frac{\text{Vol\%}_{\text{Ph.n}} \times \rho_{\text{Ph.}n}}{\sum_1^n (\text{Vol\%}_{\text{Ph.}} \times \rho_{\text{Ph.}})}\right] \quad (1)\end{aligned}$$

Equation (1) shows the modal recombination procedure used to calculate the bulk major element compositions of lithic clasts in NWA 12949. Variables are defined as follows (after Hahn et al., 2017): C is the concentration of element A of phase (Ph.) n; q the density of phase(s); and vol% the volume percent of phase(s). References for phase densities (g cm^{-3}) are taken from Klein and Dutrow (2007), that is, augite (3.30), chromite (4.60), ilmenite (4.72), merrillite (3.19), olivine (3.40), orthopyroxene (3.38), pigeonite (3.38), plagioclase (2.75), tridymite (2.65), and troilite (4.61).

Identification of Lithic Clasts

The types of lithic clasts present in NWA 12949 were identified using mineral distribution maps obtained in the Bulk Composition Reconstruction for Clasts section. Application ENVI 5.3 was then used to operate supervised classification for the types of clasts. After classification, the majority/minority analysis was conducted to eliminate small mineral breccias scattered in the metal and sulfide phases. In this study, the "ultramafic clasts" are classified as silicate clasts with low bulk SiO_2 (≤45 wt%) and MgO (≥18 wt%) contents, and composed of usually >90% mafic minerals (i.e., olivine and pyroxene), and "mafic to intermediate clasts" are classified as silicate clasts with bulk SiO_2 content between 45 and 65 wt%.

RESULTS

Modal Abundance and Classification

Mesosiderite NWA 12949 comprises ~45.0 vol% metal+sulfide phases and ~55.0 vol% silicate phases. The metal and sulfide phases contain 22.7 vol% troilite, 21.8 vol% kamacite, and 0.5 vol% taenite. The silicate phases contain 18.0 vol% orthopyroxene,

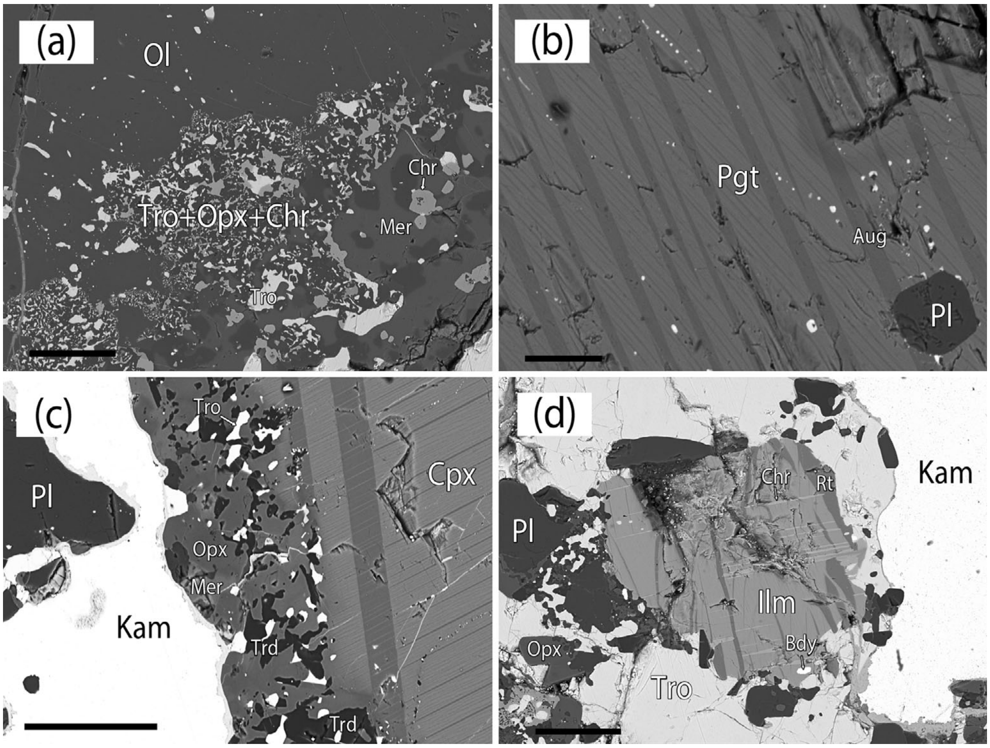

FIGURE 1. Backscattered electron images of Northwest Africa (NWA) 12949. (a) The margin of Clast I shows the reaction structure of troilite–orthopyroxene–chromite–olivine intergrowth and coexisting merrillite. (b) Two generations of pyroxene exsolution lamellae (augite exsolved from pigeonite) are present in Clast III. (c) The margin of mafic clasts, showing coronas (reaction rims) of troilite–merrillite–orthopyroxene–tridymite assemblages. (d) Fe-Ti oxides in NWA 12949. The host ilmenite contains exsolution lamellae of rutile and chromite. Baddeleyite also coexists with them. Mineral abbreviations (after Whitney & Evans, 2010): Aug, augite; Bdy, baddeleyite; Chr, chromite; Cpx, clinopyroxene; Ilm, ilmenite; Kam, kamacite; Mer, merrillite; Ol, olivine; Opx, orthopyroxene; Pgt, pigeonite; Pl, plagioclase; Rt, rutile; Trd, tridymite; Tro, troilite. The black bar in each panel indicates a scale of 50 μm.

10.4 vol% groundmass, 9.5 vol% plagioclase, 8.8 vol% pigeonite, 4.0 vol% olivine, 1.6 vol% silica (tridymite), 1.3 vol% merrillite, 0.9 vol% augite, 0.5 vol% chromite, and minor Fe-Ti oxides. The silicate phases are present as lithic clasts, discretely distributed in metal and sulfide phases. The pronounced brecciated texture, along with fine-grained (~10 μm) silicate groundmass, partial replacement of olivine, and inverted pigeonite, makes the mesosiderite NWA 12949 classified as type 2A (Floran, 1978; Hewins, 1984; Powell, 1969, 1971). The distribution of the phases in NWA 12949 is shown in Figure S1.

Petrology of Lithic Clasts

Mesosiderite NWA 12949 presents both ultramafic clasts (~18.7 modal%) and mafic to intermediate clasts (~81.3 modal%) (Figure S1). No felsic clast is found in the sample. All the locations of lithic clasts studied below have been labeled in Figure S1, and the representative petrological phenomena in these lithic clasts are shown in Figure 1.

Ultramafic Clasts

The ultramafic clasts are relatively rare (~18 modal% of lithic clasts), predominately composed of coarse-grained olivine and/or orthopyroxene. Large, euhedral chromite grains (~100–200 μm) are also observed in the ultramafic clasts. These clasts typically have diogenitic compositions, and one of them is named after Clast I (Figures 1a and 2a).

Distinct from olivine-bearing ultramafic clasts in mesosiderites recently reported (e.g., Kimura et al., 2020; Wang et al., 2010), Clast I shows some unique reaction features and mineral assemblages. Orthopyroxenes occur either at the margin of olivine or along the cracks in the interior of olivine grains; troilite and chromite grains pervasively occur within these orthopyroxenes (Figure 2b). The troilite and chromite grains are ~5 to 10 μm in size, and the orthopyroxenes are somewhat

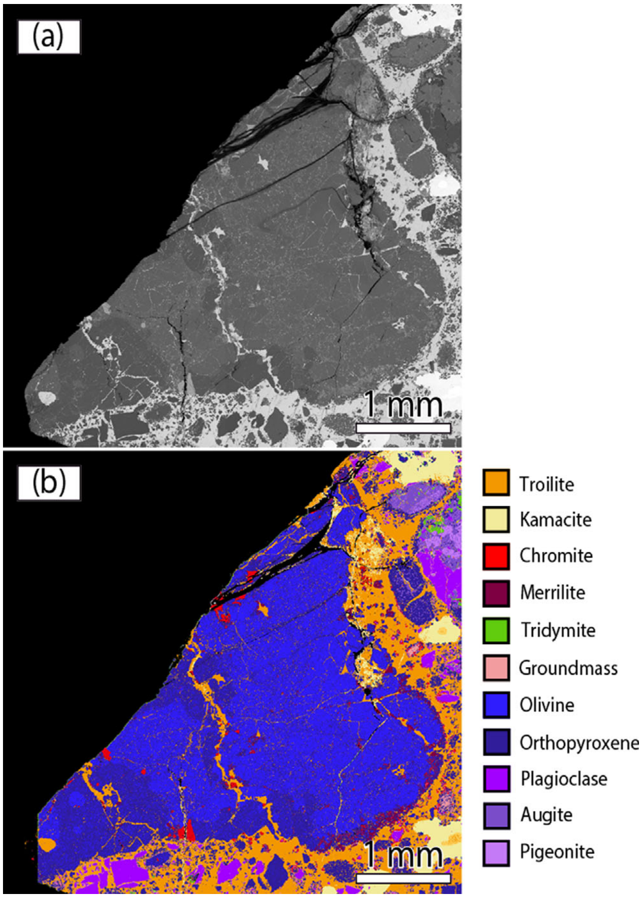

FIGURE 2. (a) Backscattered electron image of an ultramafic clast (Clast I) in mesosiderite NWA 12949. (b) The false-color phase map of Clast I.

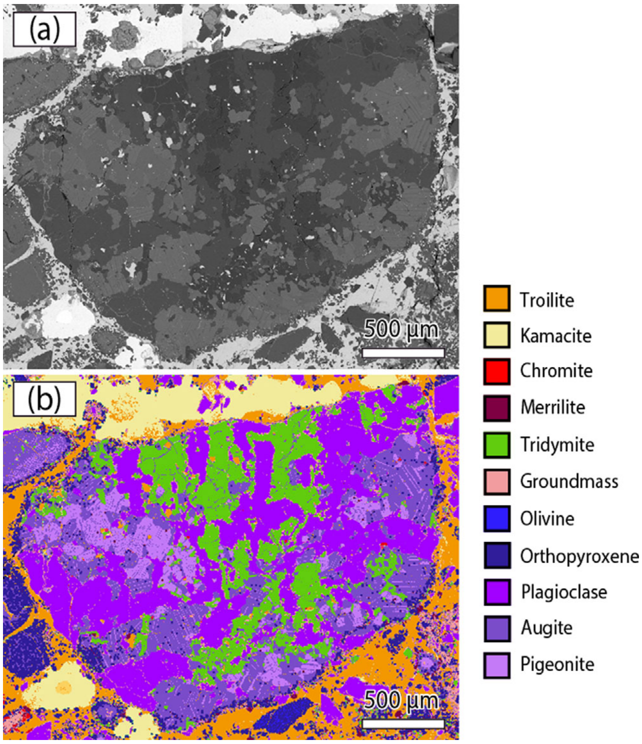

FIGURE 3. (a) Backscattered electron image of the gabbroic intermediate clast (Clast II) in mesosiderite NWA 12949. (b) The false-color phase map of Clast II.

larger (~10 to 20 µm). These three minerals compose symplectites, which partially replace olivines in Clast I (Figures 1a and 2b). The modal abundances of orthopyroxene, troilite, and chromite within the symplectite-like region are 78.3%, 11.2%, and 10.5%, respectively, exhibiting modal abundance ratios of troilite:chromite ~1, and orthopyroxene:(troilite+chromite) ~3.6. It is noted that such a symplectite-like texture exists only when the rim of the ultramafic clasts is in contact with the metal and sulfide phases. Other ultramafic clasts are relatively small (<1 mm), surrounded by fine-grained groundmass, and no symplectite texture is observed.

Mafic to Intermediate Clasts

The mafic to intermediate clasts are ubiquitous, making up the vast majority of the volume (~81.3 modal %) of lithic clasts in mesosiderite NWA 12949. The mafic to intermediate clasts are generally eucritic, except some orthopyroxene-dominant clasts are diogenitic. The mafic to intermediate clasts are present in four main types: gabbroic, poikilitic, subophitic, and cataclastic.

Gabbroic Lithology

One of the intermediate clasts (Clast II) in NWA 12949 has a medium-sized (0.3–0.6 mm in size) gabbroic texture and is mainly composed of anhedral pyroxene and equigranular plagioclase (Figure 3). Pyroxenes (~37%) are mostly pigeonite with well-developed exsolution lamellae of augite, whereas some are augite with exsolution lamellae of pigeonite (Figure 3a). In each pyroxene grain, exsolution lamellae in two directions have been found. The average width of lamellae in one direction is ~5 µm, and that in the other direction is <1 µm. The abundance of plagioclase (~39%) is almost the same as that of pyroxene. They are anhedral, medium sized (0.3–0.7 mm in size), and compositionally uniform, without chemical zoning or exsolution lamellae (Figure 3a). Silicas account for 30% of Clast II. They are anhedral tridymite with sizes of 0.2–0.5 mm (Figure 3b). Troilite (up to ~50 µm in size) and chromite (~10 µm in size) are present as accessory phases in the clast and typically fill in the shock fractures (Figure 3b).

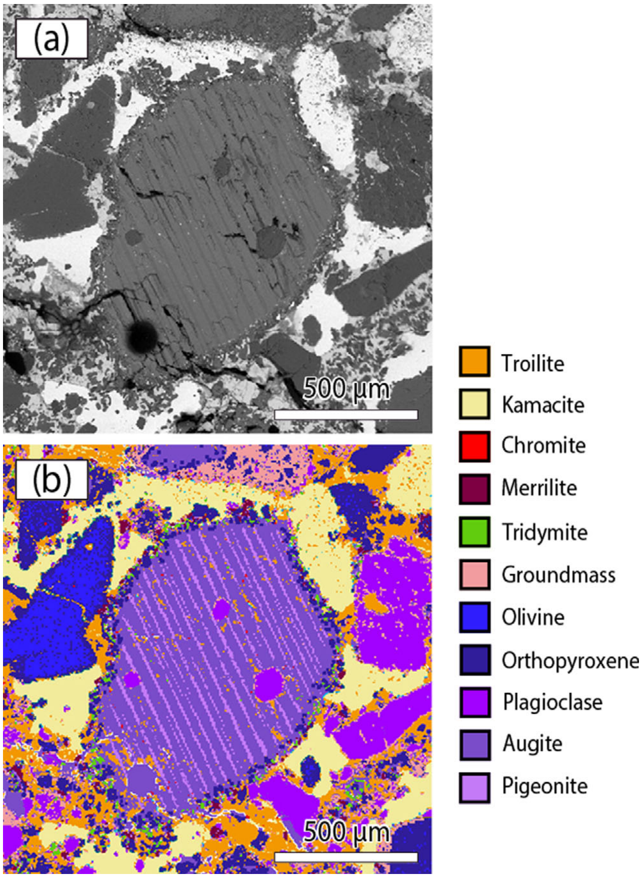

FIGURE 4. (a) Backscattered electron image of the poikilitic mafic clast (Clast III) in mesosiderite NWA 12949. (b) The false-color phase map of Clast III.

Poikilitic Lithology

Some mafic clasts in NWA 12949 are characterized by poikilitic texture where pyroxene encloses blebs of plagioclase, and one of them is shown in Figure 4, named after Clast III. The main mineral phase in Clast III is pigeonite, with augite exsolution lamellae in two directions crossing at a certain angle (Figure 1b). Lamellae in one direction are ~10 µm in average width, whereas those in the other direction are much narrower, with an average width of ~1 µm. Tridymite, merrillite, and orthopyroxene are present as coronas, or reaction rims, which are superimposed on the original pyroxene lamellae and around the Clast III (Figures 1c and 4b).

Subophitic Lithology

Some mafic clasts in NWA 12949 have a subophitic texture and are mainly composed of anhedral pyroxene and euhedral plagioclase. A representative clast is named Clast IV and is shown in Figure 5. The pyroxenes are mostly pigeonite with well-developed exsolution lamellae of augite, while some are augite with exsolution lamellae of pigeonite. Exsolution lamellae in two directions are present, and their average widths are consistent with those in Clast III (Figure 5a). Plagioclase is large, tabular, euhedral, and homogeneous, containing numerous fine-grained (<10 µm) pyroxene inclusions (Figure 5a). These anhedral pyroxene inclusions mostly show the shape of rounded blebs and are often arranged in chains and elongated along the major axis of the host plagioclase. Tridymite is concentrated in a breach of the clasts and often coexists with troilite and chromite, forming aggregates (Figure 5b).

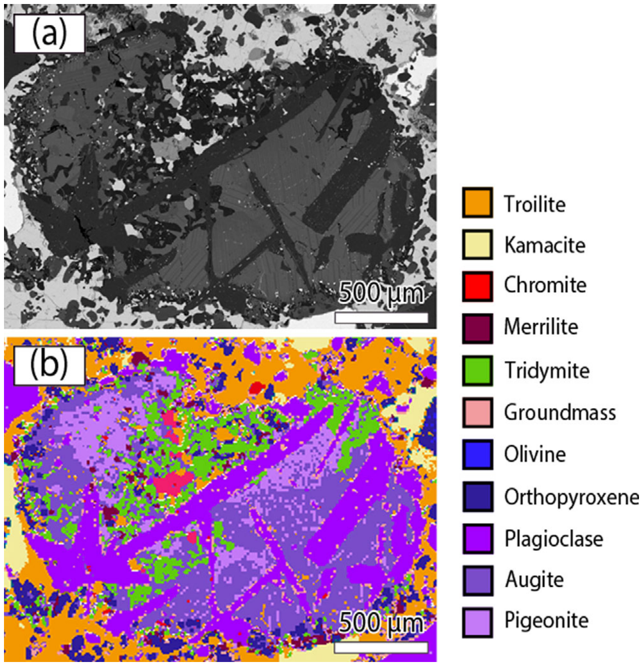

FIGURE 5. (a) Backscattered electron image of the subophitic mafic clast (Clast IV) in mesosiderite NWA 12949. (b) The false-color phase map of Clast IV.

Cataclastic Lithology

Some mafic clasts (Clast V) in NWA 12949 exhibit a cataclastic texture, that is, a mixture of orthopyroxene, clinopyroxene, plagioclase, and tridymite breccias (Figure 6). These breccias are cemented by fine-grained groundmass. Skeletal/hopper crystals are pervasively distributed in the groundmass (Figure 6a). In addition, the exsolution lamellae in pyroxene breccias have become blurred and discontinuous (Figure S3).

Fe-Ti oxide grains are also scattered in the groundmass, with a common size of <10 µm. Some Fe-Ti oxide grains are larger (50–100 µm), generally coexisting with chromite and rutile. A representative grain is shown in Figure 1d. This grain is characterized by rutile exsolution lamellae (~5–10 µm in width) and narrower chromite exsolution lamellae (<2 µm in width). The host Fe-Ti oxide grain is ilmenite. Baddeleyite is also present in the host ilmenite.

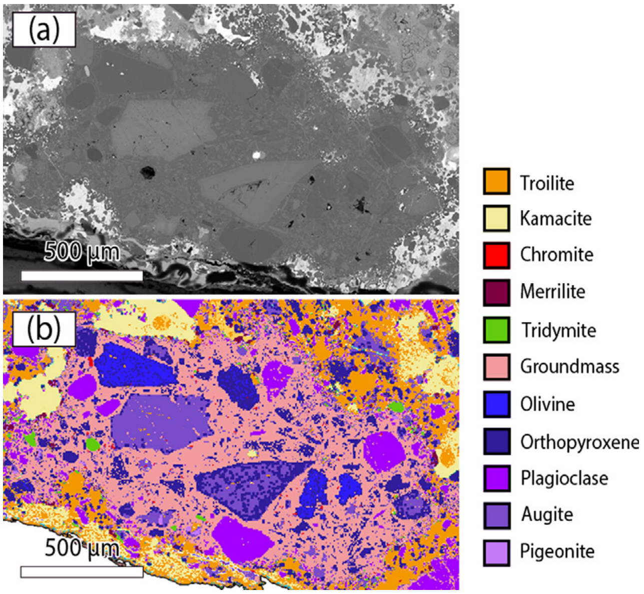

FIGURE 6. (a) Backscattered electron image of the cataclastic mafic clast (Clast V) in mesosiderite NWA 12949. (b) The false-color phase map of Clast V.

Mineralogy

Olivine

The chemical composition of olivine in mesosiderite NWA 12949 analyzed in this study is exhibited in Table 1 and File S1. There are two types of olivine in the sample, one (Ol-I) is relatively Mg poor, with Mg# (i.e., Mg/[Mg + Fe] × 100 in molar proportions) from 69 to 71; the other (Ol-II) is relatively Mg rich, with Mg# from 89 to 90. The olivine associated with symplectite-like texture belongs to Ol-I. Ol-II is rare, surrounded by fine-grained groundmass and showing no symplectite-like texture. The Fe/Mn ratios of Ol-I and Ol-II are 31–35 and 51–52, respectively, consistent with those of olivine from diogenites (32–52; Mittlefehldt, 2014).

Pyroxene

There are two groups of pyroxenes in mesosiderite NWA 12949 (Table 1 and File S1). One group is orthopyroxene ($\mathrm{Wo}_{1.36–3.26}\mathrm{En}_{67.65–77.09}\mathrm{Fs}_{21.30–29.34}$), with higher Mg# (70.5–78.9) and sometimes coexisting with olivine to form symplectite-like texture (e.g., Clast I; Figures 1a and 2a). This group falls within the region of diogenite pyroxene (Figure 7). The compositions of orthopyroxene associated with symplectite-like texture exhibit lower contents of Cr_2O_3 and Al_2O_3 (~0.1–0.6 wt% to ~0.2 to 0.7 wt%, respectively) than the typical diogenite orthopyroxene (~0.4–0.9 wt% and ~0.5–1.0 wt%, respectively).

The other group is augite ($\mathrm{Wo}_{34.96–42.90}\mathrm{En}_{27.74–31.12}\mathrm{Fs}_{26.85–36.41}$)–pigeonite ($\mathrm{Wo}_{4.79–9.97}\mathrm{En}_{31.89–37.85}\mathrm{Fs}_{54.68–60.82}$) intergrowth, with lower Mg# (44–54 for augite and 35–41 for pigeonite), represented by the pyroxene in Clast II ~ V (Figure 7). This group falls within the region of basaltic eucrite pyroxene (Figure 7). The Fe/Mn values (in molar percent) of pyroxene in NWA 12949 are 27.9–32.7, consistent with those of pyroxene in HEDs (24.2–34.4; Mittlefehldt, 2014).

Plagioclase

Plagioclase grains in NWA 12949 have rather homogeneous compositions ($\mathrm{An}_{90.66–94.80}\mathrm{Ab}_{5.02–8.02}\mathrm{Or}_{0.11–0.39}$; Table 1 and File S1) and show no igneous zoning. The plagioclases are Ca rich, with compositions ranging from bytownite to anorthite.

Chromite

In mesosiderite NWA 12949, Al-Cr spinel grains are chromite with an average Cr# (Cr/[Cr + Al] × 100% in molar percent) of ~80–82 (Table 1 and File S1). Some smaller chromite grains have Cr# as low as ~72–73. Ideally, Al-Cr spinel ($[Fe, Mg][Al, Cr]_2O_4$) with no impurity ions replacing Al and Cr will evolve along the normal trend line of Cr (in atom) = 2 – Al (in atom) (black line in Figure 8). If Ti replaces Al and Cr, spinel compositions would shift to the left of the trend line. In the Cr vs. Al diagram, most of the chromite compositions in NWA 12949 fall along the normal trend line (Figure 8), while some chromite grains contain higher TiO_2 contents (up to 5.6 wt%), thus falling far away from the line. The compositions of chromite associated with symplectite-like structure in Clast I are significantly depleted in Al_2O_3 (~1 wt%), relative to those of primary chromite grains (Al_2O_3 content of ~8–13 wt%). Nevertheless, Cr and Al in the mesosiderite NWA 12949 generally overlap the range of chromite compositions in HEDs and mesosiderites (Figure 8).

Fe-Ti Oxides

Due to limited EPMA resolution, the compositions of small Fe-Ti oxide grains, exsolved chromite lamellae, and baddeleyite grains cannot be precisely determined. Instead, the compositions of large host ilmenite and exsolved rutile lamellae are shown in Table 1 and File S1. These compositions are typical for ilmenite and rutile.

Silica

Silica in mesosiderite NWA 12949 contains minor Ti, Al, Fe, Ca, and K (Table 1 and File S1). A total of nine spectral data for three distinct silica minerals in different clasts were analyzed in this study. These spectral data have Raman peaks at 219, 297, 361, 438, and 790 cm^{-1}

TABLE 1. Average chemical compositions for representative minerals.

	Olivine		High-Mg# Px	Low-Mg# Px					Fe-Ti oxides			
	Ol-I (*n* = 14)	Ol-II (*n* = 2)	Opx (*n* = 63)	Pgt (*n* = 112)	Aug (*n* = 55)	Plagioclase (*n* = 22)	Tridymite (*n* = 2)	Chromite (*n* = 14)	Ilm (*n* = 2)	Rt (*n* = 2)	Merrillite (*n* = 1)	Mesostasis (*n* = 1)
SiO_2	37.57	40.84	54.46	49.38	49.83	45.16	98.58	0.02	0.03	0.02	n.d.	51.40
TiO_2	0.02	0.01	0.08	0.34	0.66	0.01	0.20	1.34	52.75	96.80	0.02	0.49
Al_2O_3	0.01	n.d.	0.69	0.34	0.93	34.00	0.47	9.47	0.03	0.01	0.01	15.28
Cr_2O_3	0.02	0.12	0.72	0.16	0.36	0.03	0.03	55.08	0.22	0.47	0.01	0.56
FeO	26.59	10.27	16.01	33.57	18.77	0.47	0.20	30.77	37.64	0.86	0.98	9.94
MnO	0.78	0.20	0.52	1.04	0.58	0.01	n.d.	1.38	7.33	0.09	0.51	0.42
NiO	0.02	n.d.	0.02	0.02	0.02	0.01	0.02	0.01	0.02	0.02	n.d.	0.02
MgO	35.26	48.92	26.59	11.74	10.12	0.05	n.d.	1.93	2.03	0.02	3.60	8.23
CaO	0.04	0.06	1.18	3.45	18.63	19.52	0.11	0.02	0.04	0.02	47.25	12.80
Na_2O	n.d.	0.01	0.01	0.02	0.06	0.81	0.01	0.01	n.d.	0.03	0.58	0.76
K_2O	0.01	n.d.	0.01	0.01	0.01	0.05	0.25	0.01	n.d.	0.03	0.02	0.07
P_2O_5	n.d.	n.d.	n.d.	n.d.	n.d.	n.d.	n.d.	n.d.	n.d.	n.d.	45.84	n.d.
Total	100.34	100.45	100.29	100.08	99.96	100.13	99.88	100.05	100.07	98.35	98.82	99.97
Mg#	70.3	89.5	74.6	38.4	49.2	—	—	—	—	—	—	59.6

Note: Mg# = Mg/(Mg + Fe) × 100 in molar proportions.

Abbreviations: Aug, augite; Ilm, ilmenite; n.d., not detected; Ol, olivine; Opx, orthopyroxene; Pgt, pigeonite; Rt, rutile.

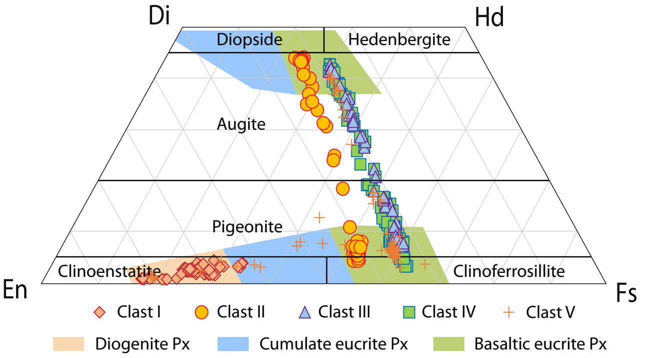

FIGURE 7. Quadrilateral pyroxene composition of pyroxenes analyzed in the lithic clasts of NWA 12949. Colored ranges of pyroxenes are from Liao and Hsu (2017) and references therein.

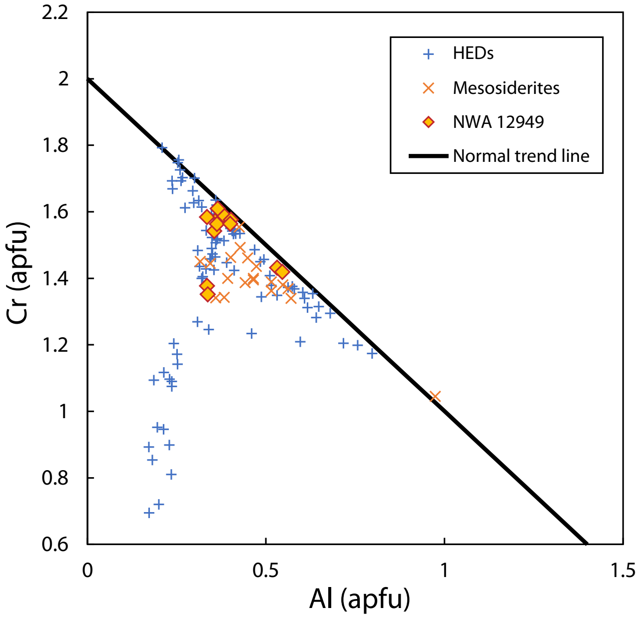

FIGURE 8. Cr versus Al diagram of spinel in NWA 12949, compared with howardite, eucrite, and diogenites (HEDs) and other mesosiderites. The normal trend line (Cr [in atom] = 2 – Al [in atom]) represents the compositions of pure Al-Cr spinel ([Fe, Mg][Al, Cr]$_2$O$_4$). The HED data are from Mittlefehldt (2014), and the mesosiderite data are from Floran et al. (1978), Mittlefehdt et al. (1998), Kong et al. (2008), and Kimura et al. (2020). apfu, atoms per formula unit.

(Figure 9), consistent with the spectral characteristics of tridymite (Cao et al., 2019).

Groundmass

The groundmass is distributed around the lithic clasts in NWA 12949 (Figure 6a; Figure S1), with compositions analogous to the mixture of plagioclase and pyroxene (Table 1 and File S1).

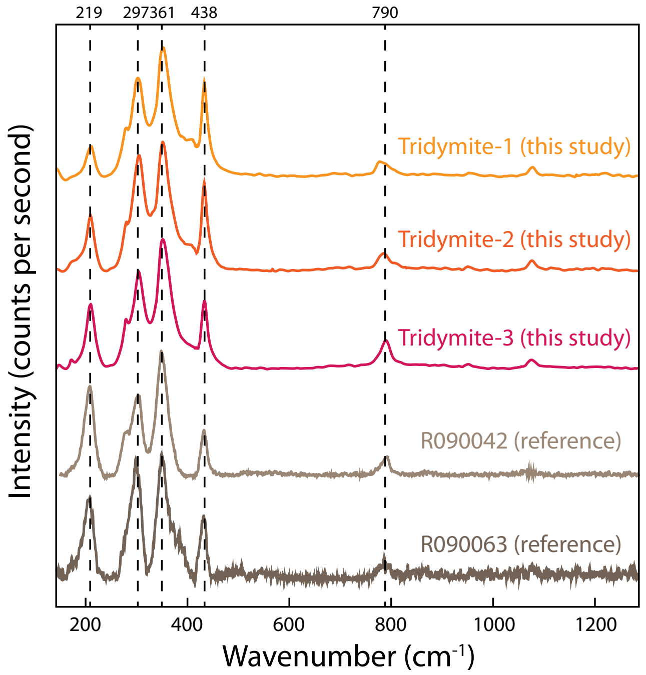

FIGURE 9. The Raman spectra of silica in NWA 12949, compared with references R090042 and R090063 (from the Raman Spectroscopy Database, RRUFF).

DISCUSSION

Petrogenesis of Clast II

Clasts III and IV have pyroxene Fe/Mn ratios (28.7–32.9) indistinguishable from those of eucrites (25.4–35), whereas slightly deviant from those of mesosiderites (18.5–28.3). The lithologies of Clasts III and IV are also much consistent with eucrites, as poikilitic and subophitic structures are common in eucrites and eucritic clasts in howardites (e.g., Mittlefehldt, 2015; Yamaguchi et al., 2009). However, Clast II is somewhat anomalous, with lower pyroxene Fe/Mn (~28.3 on average, some as low as ~20) and Fe/Mg (~1–1.3 on average, some as low as ~0.5) than other lithic clasts in NWA 12949. The gabbroic lithology and the high silica abundance (~22%) of Clast II are also distinct from eucrites, which usually have little silica (e.g., Mayne et al., 2009).

A plausible explanation for the formation of Clast II is that it represents a source rock different from other lithic clasts. The large Fe/Mn data spread of Clast II is possibly due to the low precision of the data, which could lead to an 1σ error of ±1.2% at the current EPMA conditions (Mittlefehldt, 2005). The high abundance of tridymite is likely due to sampling bias, or post-crystallization process, for example, solid-state reaction and small degrees of partial melting (e.g., Haba et al., 2019; Yamaguchi et al., 2002). The gabbroic lithology and the lower Fe/Mn values of Clast II are close to the case of cumulate eucrites (with Fe/Mn values of 25–32; Mayne et al., 2009). However, the Fe-Mg systematics of pyroxene in Clast II fall within the region of basaltic eucrite pyroxenes (Figure 7). Besides, no sample with a composition akin to the case of Clast II has been reported before. These arguments suggest that Clast II has originated from a distinct source rock from other lithic clasts in NWA 12949, and possibly undergone different thermal processes.

To explore the thermal processes of Clast II, we modeled the evolution history of an initial magma with an average composition of the groundmass (representing recrystallized magma) in NWA 12949 at both equilibrium and fractional modes using rhyolite-MELTS (Ghiorso & Gualda, 2015; Gualda et al., 2012). The modeling results show that the major element compositions of Clast II can be reproduced after ~70–75 wt% crystallization of the initial magma (Figure 10). However, the bulk compositions of other mafic clasts do not fall within the evolution trends of the initial magma. This supports the possibility that Clast II can be derived from the recrystallized mesostasis of a parent body, and does not share a common parent magma with other mafic clasts. The interpretation for the petrogenesis of Clast II again indicates that the lithic fragments in NWA 12949 are unlikely to originate from a common pristine source rock, and multiple sources or geological processes are needed for explicating the diversity of the fragments.

Metamorphic Reactions

Reactions in Olivine

In Clast I, the large olivine grain is partially replaced by orthopyroxene, which is in equilibrium with the host olivine. Fine-grained troilite and chromite distribute pervasively in the orthopyroxene crystals (Figure 1a), indicating that the orthopyroxene–troilite–chromite symplectite-like intergrowth probably formed simultaneously. Such a symplectite-like structure has been previously found in various meteorite groups, including acapulcoites (El Goresy et al., 2005), brachinites (Goodrich et al., 2011, 2017; Irving et al., 2013; Rumble et al., 2008), ungrouped achondrites (Petaev & Brearley, 1994), HEDs (Patzer & McSween, 2012; Zhang et al., 2018, 2020), mesosiderites (Lorenz et al., 2010; Ruzicka et al., 1994), Apollo lunar sample (Lindstrom & Salpas, 1983; Norman, 1981), and ordinary chondrites (Li et al., 2021).

The symplectite-like structure is exhibited in the rim regions of the olivine in contact with the metal and sulfide phases, whereas olivine surrounded by fine-grained groundmass shows no symplectite-like texture. Therefore, the formation of the symplectite-like structure is likely due to the substances exsolved from the metal and sulfide phases. The most plausible explanation for the formation scenario is the sulfidation of primary olivine by S_2 vapors (Li et al., 2021; Zhang et al., 2020). S_2 has low solubility in metal and would have been progressively excluded from the crystallizing metal during cooling, leading to an enrichment in the residual metallic melt (Wasson, 1999; Williams et al., 2006). Furthermore, the reaction of olivine and S_2 vapor was experimentally confirmed by Kullerud and Yoder (1963). At high temperatures (~1000 °C), S_2 vapor can react with olivine, removing FeO in olivine and forming orthopyroxene through the reaction:

$$2(\mathrm{Fe,Mg})_2\mathrm{SiO}_4 + \mathrm{S}_2 \rightarrow 2\mathrm{MgSiO}_3 + 2\mathrm{FeS} + \mathrm{O}_2(\mathrm{g}). \quad (2)$$

The presence of chromite in Clast I may be due to primary crystallization or post-reaction (e.g., Mittlefehldt, 2015; Ruzicka et al., 1994). Large chromite grains are more likely to have a primary origin, as they are euhedral and isolated from the symplectite-like texture. However, the small, scattered chromite grains, associated with symplectite-like texture, are clearly Al_2O_3-depleted relative to primary chromite grains. These chromite grains may be derived from the chemical reaction of olivine with S_2 and Cr_2O_3, based on the following reaction equation (e.g., Ruzicka et al., 1994; Vaci et al., 2021):

$$\begin{array}{ll} 6(\mathrm{Fe,Mg})_2\mathrm{SiO}_4 + 5\mathrm{S}_2 + 2\mathrm{Cr}_2\mathrm{O}_3 \rightarrow & \\ \quad 6\mathrm{MgSiO}_3 + 4\mathrm{FeS} + 2\mathrm{FeCr}_2\mathrm{O}_4 + 2\mathrm{O}_2(\mathrm{g}) & \\ \text{Olivine} \qquad \text{Orthopyroxene Troilite Chromite.} & (3) \end{array}$$

The original Cr content dissolved in mesosiderite kamacite is possibly ~0.3 wt% (Ruzicka et al., 1994). Besides, Equation (3) involves olivine as the silicate reactant, which contains up to 0.12 wt% Cr_2O_3 in NWA 12949 (File S1). Therefore, the Cr_2O_3 may form through the exsolution and oxidation of Cr from the metal during cooling, or originate from silicate portions during the metamorphic reaction.

Equation (3) synthesizes the reaction of olivine with sulfur and Cr_2O_3. Specifically, as indicated by Zhang et al. (2018, 2020), the form of reaction equations in NWA 12949 could be:

$$\begin{array}{l} 100\mathrm{Mg}_{1.41}\mathrm{Fe}_{0.59}\mathrm{SiO}_4 + 3\mathrm{S}_2 + 6\mathrm{Cr}_2\mathrm{O}_3 + 88\mathrm{SiO}_2 \rightarrow \\ 188\ \mathrm{Mg}_{0.75}\mathrm{Fe}_{0.25}\mathrm{SiO}_3 + 6\mathrm{FeS} + 6\mathrm{FeCr}_2\mathrm{O}_4 + 3\mathrm{O}_2, \quad (4) \end{array}$$

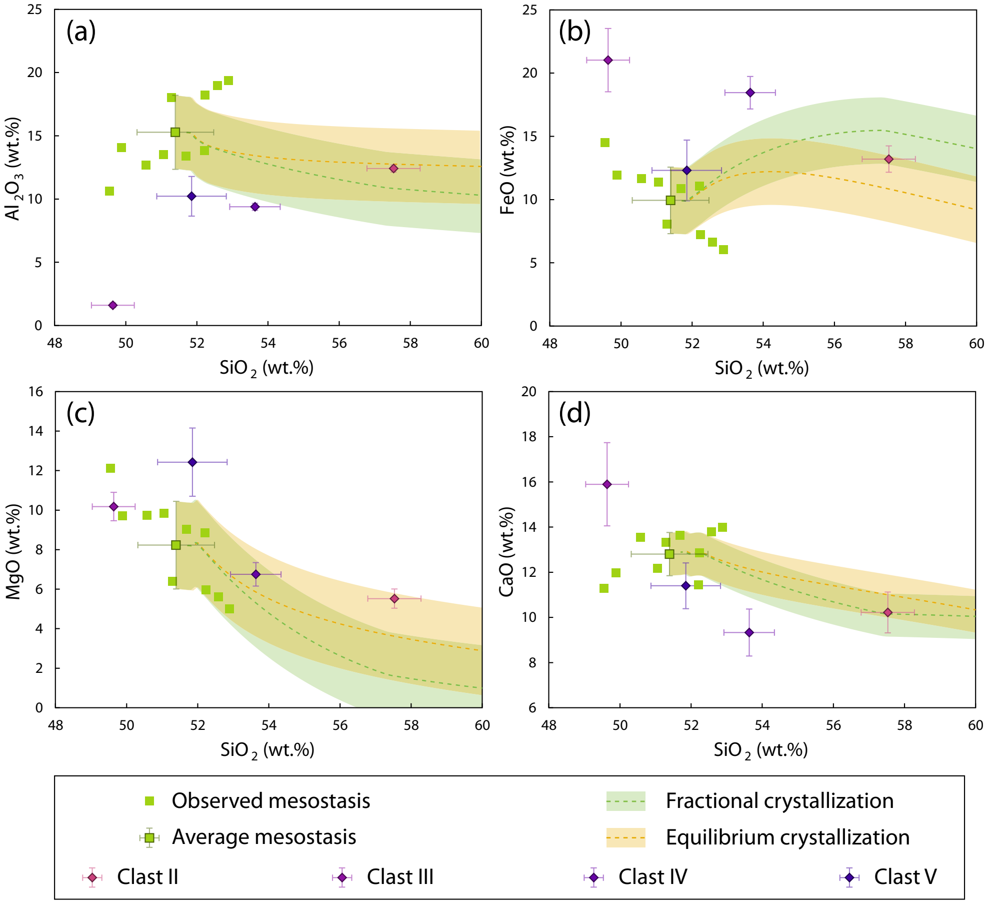

FIGURE 10. Harker diagrams for the compositions of the groundmass (green squares) and lithic clasts (purple diamonds) in NWA 12949. (a) Bulk Al_2O_3 contents vs. bulk SiO_2 contents; (b) bulk FeO contents vs. bulk SiO_2 contents; (c) bulk MgO contents vs. contents vs. bulk SiO_2 contents; (d) bulk CaO contents vs. bulk SiO_2 contents. The calculated trends from the MELTS modeling discussed in the text for the average composition of the groundmass are shown in colored curves. Error bars are 1σ.

or

$$200Mg_{1.41}Fe_{0.59}SiO_4 + 17S_2 + 34Cr_2O_3 \rightarrow 200\,Mg_{0.75}Fe_{0.25}SiO_3 + 34FeS + 34FeCr_2O_4 + 132MgO + 17O_2. \quad (5)$$

Both of the two reactions produce the modal ratio of troilite and chromite of ~1, consistent with the observed troilite/chromite modal ratio. However, the products of reaction Equation (4), that is, orthopyroxene and metal-compound phases (troilite+chromite), have a modal ratio of ~16, while those of the reaction Equation (5) have a modal ratio of ~3. Considering the observed modal ratio of ~3.6 (Figure 1a), the reaction Equation (5) is more likely for the case of NWA 12949. This interpretation is also consistent with Zhang et al. (2020), who reported a similar symplectite-like texture in diogenite. Therefore, the olivine can react with S_2 and Cr_2O_3 exsolved from the metal during the reheating of metal–silicate mixing, forming excess troilite and chromite observed in mesosiderite NWA 12949.

Reactions in Pyroxene

Pyroxene coronas, which manifest high-temperature (850–1100 °C) metamorphism (Harlow et al., 1982; Ruzicka et al., 1994), are present in all the mafic to intermediate clasts of NWA 12949. These coronas are characterized by fine-grained orthopyroxene, troilite, tridymite, and merrillite assemblages (Figure 1c), clearly formed by a reaction between pyroxene and reducing substances in the metal.

We noticed that the pyroxene grains in coronas have remarkably lower Fe/Mg (~0.5–1) and Fe/Mn (~20–25) compared with the pyroxenes within clasts (Fe/Mg ~1–1.8 and Fe/Mn ~30) (Figure 11). This was explained by the Fe removal of silicates through pervasively redox reactions in the metal–silicate thermal mixture (Mittlefehldt, 1990). Specifically, Fe and Mn have fairly similar partition coefficients under relatively reducing

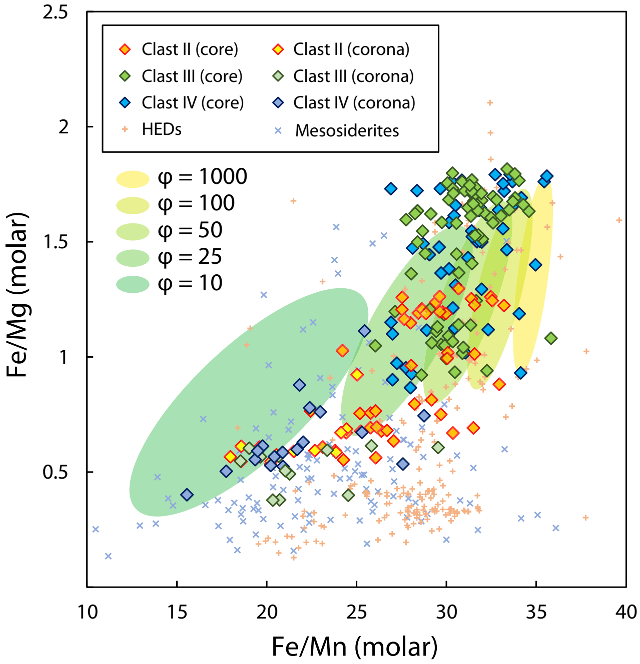

FIGURE 11. Pyroxene Fe/Mg versus Fe/Mn diagram of lithic clasts in NWA 12949; howardite, eucrite, and diogenites (HEDs); and other mesosiderites. φ is the reaction coefficient (see the text). This diagram indicates the effect of initial S_2 content on pyroxene Fe/Mg and Fe/Mn variations. The measurement error of Fe/Mn ratios is ±1.2% at the current EPMA conditions (Mittlefehldt, 2005). The HED data are from Mittlefehldt (2015). The mesosiderites data are from Floran et al. (1978), Hewins (1979), Kimura et al. (1991, 2020), Mittlefehldt et al. (1998), Wang et al. (2010), and Kong et al. (2008).

conditions and are partitioned between crystal and liquid (Goodrich & Delaney, 2000; Papike et al., 2003). However, the partition of Fe and Mn differs slightly and is sensitive to changes in redox conditions: FeO reduces to metal under many circumstances relevant to planetary magmatism, while MnO does not reduce in most meteoritic systems (Delaney et al., 1981; Mittlefehldt, 1990). Hence, such a discrepancy is likely to result from redox reactions between pyroxene and reducing substances (mostly S_2) in the molten metal. The reaction equation between pyroxene ($Ca_xMg_yFe_{1-x-y}SiO_3$) and S_2 is

$$(\varphi+2)Ca_xMg_yFe_{1-x-y}SiO_3 + 2S_2 \rightarrow \varphi Ca_{\frac{\varphi+2}{\varphi}x}Mg_{\frac{\varphi+2}{\varphi}y}Fe_{1-\frac{\varphi+2}{\varphi}(x+y)}SiO_3 + 2FeS + 2SiO_2 + O_2, \qquad (6)$$

where φ is the reaction coefficient, reflecting the “excess level” of reactant pyroxene relative to sulfur. The lower the φ value, the more excessive sulfur relative to pyroxene, and the more effective removal of FeO from pyroxene. Calculations show that if pyroxene with an initial Fe/Mg of ~0.9–1.8, initial Fe/Mn of ~34–35, when φ = 100, the Fe/Mg would decrease to ~0.8–1.7, and the Fe/Mn would decrease to ~31–34; when φ = 10, the Fe/Mg would decrease to ~0.3–1.3, and the Fe/Mn would decrease to 13–25 (Figure 11). For NWA 12949, the best fit of φ is ~20, that is, the reactant ratio (pyroxene/S_2 in molar) is ~11 (Figure 11). These effects of redox reaction are similar to the case of ureilites, which have olivine grains with Mg- and Mn-rich rims due to CHOS gas/fluid-induced reductions (e.g., Langendam et al., 2021).

The presence of fine-grained merrillite ($Ca_5NaMg[PO_4]_7$) and tridymite has also been attributed to redox reactions in the pyroxene coronas in mesosiderites by oxidation of P contained in the metal (Delaney et al., 1981; Fuchs, 1969; Harlow et al., 1982; Mittlefehldt, 1990; Nehru et al., 1978; Powell, 1971). In mesosiderites, P is initially dissolved in metal proportion and stays in metal at high temperatures (>1100 °C) (Harlow et al., 1982; Sugiura et al., 2019). Agosto et al. (1980) and Harlow et al. (1982) have found that coexisting P-bearing Fe-Ni metal and clinopyroxene in mesosiderite should have reacted during cooling at around 1000 °C to produce the observed merrillite and much of the tridymite as well as excess metallic Fe. The generated metallic Fe further reacts with S_2 exsolved from the metal to form the observed troilite. The total reaction equation is as follows:

$$\underset{\text{Clinopyroxene}}{20CaMgSi_2O_6 + 86FeSiO_3} + 2Na_2O + 28P + 43S_2 \rightarrow \underset{\text{Merrillite}}{4Ca_5NaMg(PO_4)_7} + \underset{\text{Orthopyroxene}}{16MgSiO_3} + \underset{\text{Tridymite}}{110SiO_2} + \underset{\text{Troilite}}{86FeS}. \qquad (7)$$

The redox reactions between reducing substances (S_2 and P) and silicates are pervasively recorded in mesosiderites (e.g., Delaney et al., 1981; Harlow et al., 1982) and may provide important information to unravel the link between mesosiderites and HEDs. In NWA 12949, all the pyroxene crystals in the cores of mafic to intermediate clasts, except those in Clast II, have Fe/Mn ratios (~30) identical to HEDs. The redox reactions between S_2/P and pyroxene have significantly affected pyroxene compositions in the rims of mafic to intermediate clasts, forming low Fe/Mn (as low as ~20) pyroxene in the coronas, thus much more akin to those in mesosiderites previously reported. Besides, the redox reactions between S_2/P and HED-like materials produce excess phosphates and silica, consistent with the higher modal abundance of these species in mesosiderites than HEDs, for example, phosphate concentration in mesosiderites is five times higher than in eucrites and howardites (Powell, 1971), and the average modal abundance of tridymite is ~8% in mesosiderites (McCall, 1966), while only 4% in eucrites (Delaney et al., 1981). This supports the model that redox reactions can bridge the gap between mesosiderites and HEDs (Caves, 2019). Finally, by combining the Fe/Mn similarity between pyroxene in eucrites and pyroxene without being affected by the redox reaction in lithic clasts of NWA 12949, the lithic clasts in mesosiderite NWA 12949 may have the same origin with HEDs, that is, asteroid 4 Vesta. In summary, all the discrepancies in Fe/Mn ratios, Fe/Mg ratios, and modal abundances of silicates and phosphates between mesosiderites NWA 12949 and HEDs may be explained by varying degrees of redox reactions between S_2/P and silicates, which are driven by decoupling of S_2/P and molten metal during metal–silicate mixing.

Thermal Equilibrium Temperatures

A conspicuous characteristic is that the lithic clasts in NWA 12949 have pervasively gone through thermal events. The chemically homogeneous minerals, pyroxene exsolution lamellae, and coexisting reaction-related mineral assemblages are the results of partial equilibration reached in prolonged thermal events. Hence, the thermal equilibrium temperatures can be determined by these textures.

Equilibrium temperatures of coexisting lamellae and host pyroxene in mafic clasts (e.g., Figure 1b) of mesosiderite NWA 12949 were calculated using a series of pyroxene geothermometers. The geothermometers provide a temperature of 907 ± 15 °C (Wells, 1977), 882 ± 19 °C (Taylor, 1998), 900 ± 24 °C (Putirka, 2008), and 908 ± 19 °C (Nakamuta et al., 2017) between the lamellae and their host pyroxene. The calculated equilibrium temperatures are similar to basaltic eucrites (e.g., Schwartz & McCallum, 2005; Yamaguchi et al., 1996) and eucritic clasts in other mesosiderites (e.g., Pittarello et al., 2019).

The ultramafic clasts have coexisting olivine, orthopyroxene, and chromite assemblages (Figures 1a and 2), which can also be used to constrain the peak temperatures of thermal equilibration. The equilibrium temperature of orthopyroxene–olivine assemblages in Clast I is ~1000 °C, using the isothermal contours constructed by Shearer et al. (2010). The aluminum-in-olivine thermometry (Coogan et al., 2014), which calculates the equilibrium temperature between coexisting olivine and chromite, gives a temperature range of 1080 ± 25 °C. In addition, the equilibrium temperature between the coexisting olivine, orthopyroxene, and chromite in Clast I was calculated to 1005 ± 35 °C at 1–1000 bar, using the QUILF program of Andersen et al. (1993). Therefore, these geothermometers indicate a consistent equilibrium temperature of ~1000–1100 °C for the ultramafic clasts in NWA 12949.

The different equilibrium temperatures indicate that the peak metamorphic temperature has ever reached > ~1000–1100 °C for ultramafic clasts, and > ~880–910 °C for mafic to intermediate clasts. Hence, the ultramafic clasts may have undergone an igneous process with a somewhat higher temperature. If it is the case, the results would be consistent with the relative formation depths of eucrites and diogenites, that is, the diogenites are considered to be derived from the middle–lower crust while eucrites from the upper crust, thus the diogenites typically record higher equilibrium temperatures (e.g., Mittlefehldt, 2015). This consistency also supports the HED origin of lithic clasts in NWA 12949.

Cooling Rate Estimations

A common method to estimate the cooling rates is elemental diffusion calculations. The cooling processes after each thermal event would inevitably produce chemical zoning in silicate minerals (e.g., olivine, pyroxene, and plagioclase) due to thermal diffusion, similar to that observed in unequilibrated eucrites (e.g., Takeda & Graham, 1991). The cooling rate can thus be numerically calculated by solving thermal diffusion equations. However, this method does not apply to the case of NWA 12949, as the primary zoning in its silicate minerals has been thoroughly erased by subsequent long-lived thermal equilibration.

An alternative method to evaluate the cooling rates is based on the thickness of exsolution lamellae in pyroxene, controlled by the cooling rates (e.g., Pittarello et al., 2019). Utilizing this method, Miyamoto and Takeda (1977) have composed the relationship between the cooling rate and the thickness of pyroxene exsolution lamellae parallel to (001) in eucrites. The two directions of exsolution lamellae of pyroxene observed in NWA 12949, that is, lamellae with composition planes close to (001) and those close to (100), are considered to be formed by monotonous cooling in the same thermal event (e.g., Ishii & Takeda, 1974; Müller, 1993). The average thickness of pyroxene lamellae in poikilitic–subophitic clasts of NWA 12949 (e.g., Clast III and IV) is ~10 μm wide, thus corresponding to a cooling rate of ~0.0044 °C year^{-1}. The calculated cooling rate is rather low, suggesting that the clasts have been emplaced deep in the regolith of the parent asteroid after crystallization. Using the cooling rate–burial depth relationship in Miyamoto and Takeda (1977), the burial depth is estimated to be 1.7 km. Pyroxene grains in Clast II have somewhat thinner exsolution lamellae (~5 μm), corresponding to a cooling rate and a burial depth of

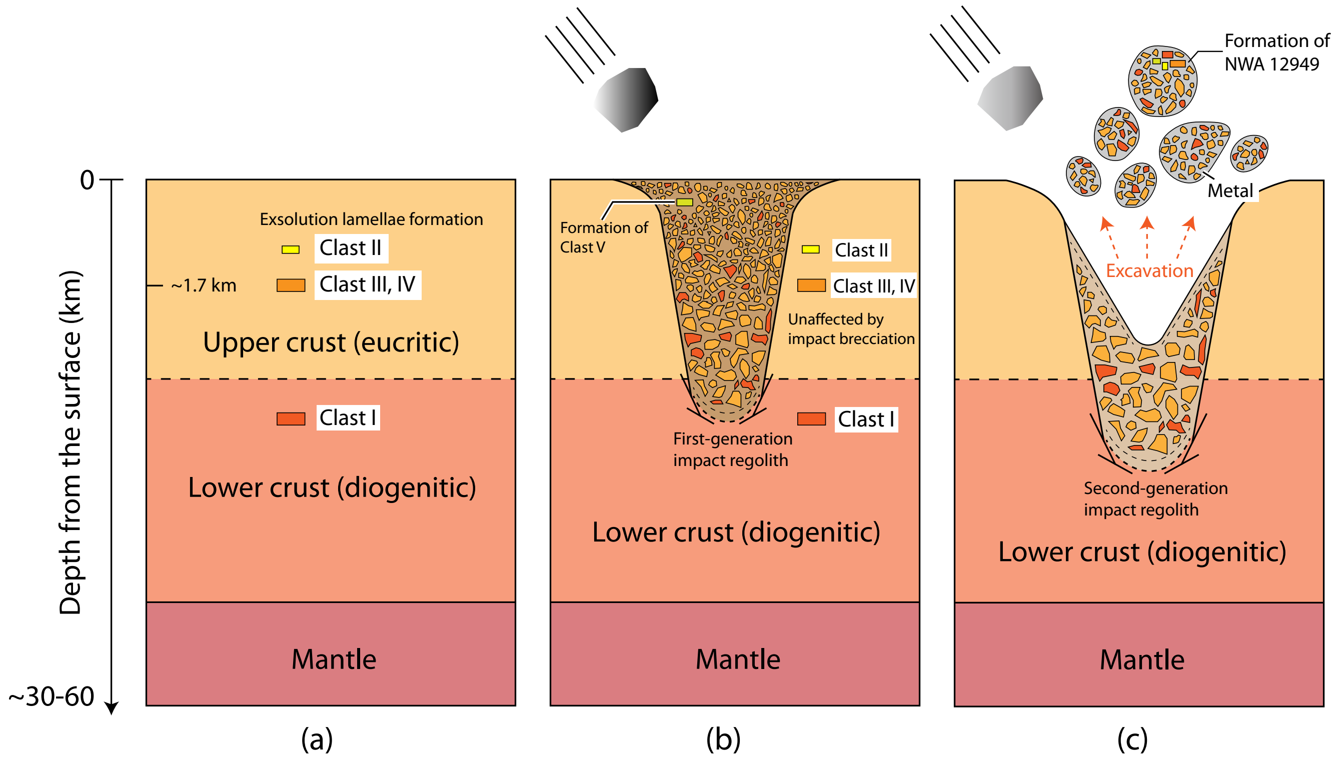

FIGURE 12. Formation of mesosiderite NWA 12949 on 4 Vesta. (a) Initial crystallization of the mesosiderite silicates, formed Clast I, as well as Clasts II, III, and IV. (b) The first impact reheating event caused a large-scale disruption of the upper and lower crust, forming Clast V. (c) Second impact reheating event caused metal–silicate mixing and the ultimate formation of mesosiderite NWA 12949. It is uncertain whether the collision disrupted the asteroid core or not, that is, the origin of metal came from 4 Vesta or the exogenic impactor.

~0.018 °C year^{-1} and ~0.84 km, respectively. However, as noted by Pittarello et al. (2019), these results should be used very cautiously, as the thickness of lamellae is potentially controlled also by other factors, for example, exsolution temperatures (Miyamoto et al., 2001; Sugiura & Kimura, 2015).

The petrology of melt breccia clasts in NWA 12949 (e.g., Clast V) seems to indicate much faster cooling rates than the poikilitic–subophitic clasts. The presence of skeletal/hopper crystals, fine-grained groundmass, and angular mineral breccias all suggest a rapid cooling rate of at least a few °C per hour (e.g., Bouquain et al., 2014; Faure et al., 2003; Mikouchi et al., 2003), 5–8 orders of magnitude faster than the estimated cooling rates in poikilitic–subophitic clasts (0.0044–0.018 °C year^{-1}). The melt breccia clasts are thus emplaced at the chilling surface of the parent asteroid. Such a clear difference in cooling rates indicates distinct geological histories between the poikilitic–subophitic clasts and the melt breccia clasts. The coexistence of the clasts with significantly different cooling rates in NWA 12949 possibly indicates that the impact processes could effectively mix the parent asteroid materials at different depths (from the surface to at least ~1.7 km deep) to form breccias.

Plausible Geological History for NWA 12949

The source rocks of lithic clasts were generally believed to be formed by the primary crystallization of parent magma at the early stage (e.g., Miyamoto et al., 2001; Takeda & Mori, 1985). The varying grain sizes and extents of exsolution lamellae in pyroxene reflect a range of cooling environments (Powell, 1971). Hence, the source rocks of Clast III and IV in NWA 12949 were probably formed during slow cooling (~0.0044 °C year^{-1} to ~880–910 °C), within a shallow intrusion (~1.7 km depth). The source rock of Clast II was possibly formed with a somewhat higher cooling rate (~0.018 °C h^{-1}), corresponding to a distinct source region. The source rock of Clast I is ultramafic and probably located in the lower crust of the parent body. This process is interpreted as event 1 in this study (Figure 12a).

After the initial crystallization of the silicates, impact events caused extensive brecciation resulting in cataclastic features of some source rocks. The impact and concomitant thermal event reheated the cataclastic rocks, resulting in shock-induced melting, as well as post-reaction and reabsorption between lamellae and host pyroxene, which are evidenced by the blurred exsolution lamellae of pyroxene in Clast V (Figures 6 and S3). The shock melt was buried by impact-induced regolith and recrystallized, forming the fine-grained groundmass and skeletal/hopper crystals between breccias in Clast V. This process is interpreted as event 2 in this study (Figure 12b).

Eventually, another impact event resulted in reheating and metal–silicate mixing. The elevation of temperatures above 1000–1100 °C initiated the redox reactions between silicate clasts and reducing substances (i.e., P and S_2), followed by the homogenization and re-equilibration of coexisting minerals as cooling slowly proceeded. This metamorphic process is evidenced by the petrological observations that symplectite-like metamorphic texture has been superimposed on the rim of the clasts in contact with metal and sulfide phases (Figures 1a and 2), which indicates that the onset of redox reactions commenced after the formation of brecciated clasts and groundmass. The impact event mixed the clast breccias at different burial depths, forming Clasts I–IV and leading to an overall howarditic lithology of silicate fraction of NWA 12949. This process is interpreted as event 3 in this study (Figure 12c).

The scenario is coincidentally consistent with the model proposed by Metzler et al. (1995), Patzer et al. (2003), and Gardner-Vandy et al. (2011) to account for the origin of HEDs. However, this scenario is only one of the plausible models involving mesosiderite formation. We cannot distinguish the total amount of impact and thermal metamorphism events and the metamorphic extent of each event; however, each event aforementioned represents at least one major impact event.

A plausible parent asteroid of mesosiderite NWA 12949 is thus 4 Vesta. The process of metal–silicate mixing and subsequent redox reactions formed lithic and mineral clasts with low Fe/Mn and Fe/Mg, high-modal abundances of tridymite, merrillite, and/or chromite. However, we do not advocate that all the mesosiderites originated from 4 Vesta, but at least some mesosiderites akin to NWA 12949 may be closely associated with 4 Vesta.

CONCLUSIONS

We conclude the following based on our studies:

1. NWA 12949 is a type 2A mesosiderite.
2. The silicate fraction of NWA 12949 is polymict, containing ultramafic, mafic, and intermediate clasts. Four types of mafic to intermediate clasts are present in NWA 12949: gabbroic, poikilitic, subophitic, and cataclastic.
3. The pyroxene in mafic to intermediate clasts in NWA 12949 has a Fe/Mn and Fe/Mg indistinguishable from eucrites. The compositions of other minerals are typical of mesosiderites.
4. The silicate fraction has undergone extensive thermal metamorphism induced by redox reactions between olivine/pyroxene and S_2 and P. Based on the reaction stoichiometry, the reactant pyroxene/S_2 ratio is ~11.
5. The equilibrium temperature recorded by pyroxene lamellae and olivine–orthopyroxene–chromite assemblages are ~880–910 °C and ~1000–1100 °C, respectively.
6. Pyroxene in most mafic to intermediate clasts has exsolution lamellae in two distinct directions. The cooling rates calculated from the lamellae widths are ~0.0044 °C year^{-1} for the poikilitic–subophitic clasts, and ~0.52 °C year^{-1} for the gabbroic clast, respectively, corresponding to the burial depths of ~1.7 and ~0.84 km, respectively.
7. To form the observed petrology and mineralogy in NWA 12949, our model presented here favors that the mesosiderite parent body has gone through at least two major impact events.
8. NWA 12949 may originate from 4 Vesta. The petrographic and mineralogical differences between lithic clasts in NWA 12949 and eucrites can be explained by the different degrees of thermal metamorphism resulting from metal–silicate mixing.

Acknowledgments—The authors thank Ai-Cheng Zhang and an anonymous reviewer for their thorough and constructive suggestions, and thank Akira Yamaguchi for his constructive comments and detailed editorial works. The authors also thank Haiping Ren, Xiaoli Li, and Ying Cui for assisting with TIMA, EPMA, and Raman analysis. This research was financially supported by the National Natural Science Foundation of China (grant number 42272348).

Conflict of Interest Statement—The authors declare that they have no conflict of interest.

Data Availability Statement—The data that support the findings of this study are available in the supplementary material of this article.

Editorial Handling—Dr. Akira Yamaguchi

REFERENCES

Agosto, W. N., Hewins, R. H., and Clarke, R. S. Jr. 1980. Allan Hills A77219-The First Antarctic Mesosiderite. 11th Lunar and Planetary Science Conference, pp. 1027–45.

Andersen, D. J., Lindsley, D. H., and Davidson, P. M. 1993. QUILF: A Pascal Program to Assess Equilibria among Fe-Mg-Mn-Ti Oxides, Pyroxenes, Olivine, and Quartz. *Computers & Geosciences* 19: 1333–50.

Binzel, R. P., and Xu, S. 1993. Chips Off of Asteroid 4 Vesta: Evidence for the Parent Body of Basaltic Achondrite Meteorites. *Science* 260: 186–91.

Bogard, D. D. 2011. K–Ar Ages of Meteorites: Clues to Parent-Body Thermal Histories. *Geochemistry* 71: 207–26.

Bogard, D. D., and Garrison, D. H. 1998. ^{39}Ar-^{40}Ar Ages and Thermal History of Mesosiderites. *Geochimica et Cosmochimica Acta* 62: 1459–68.

Bogard, D. D., and Garrison, D. H. 2003. ^{39}Ar-^{40}Ar Ages of Eucrites and Thermal History of Asteroid 4 Vesta. *Meteoritics & Planetary Science* 38: 669–710.

Bogard, D. D., Garrison, D. H., and Mittlefehldt, D. 1990. ^{39}Ar-^{40}Ar Dating of Mesosiderites: Evidence for Major Parent Body Disruption <4 Ga Ago. *Geochimica et Cosmochimica Acta* 54: 2549–64.

Bouquain, S., Arndt, N. T., Faure, F., and Libourel, G. 2014. An Experimental Study of Pyroxene Crystallization during Rapid Cooling in a Thermal Gradient: Application to Komatiites. *Solid Earth* 5: 641–50.

Cao, H. J., Chen, J., Fu, X. H., and Ling, Z. C. 2019. Raman and Infrared Spectroscopic Perspectives of Lunar Meteorite Northwest Africa 4884. *Journal of Raman Spectroscopy* 51: 1652–66.

Caves, L. R. 2019. Mesosiderite Formation: Redox from the Metal Perspective. MPhil Thesis, Texas Christian University, Fort Worth, TX, USA.

Consolmagno, G. J., and Drake, M. J. 1977. Composition and Evolution of the Eucrite Parent Body: Evidence from Rare Earth Elements. *Geochimica et Cosmochimica Acta* 41: 1271–82.

Coogan, L. A., Saunders, A. D., and Wilson, R. N. 2014. Aluminum-in-Olivine Thermometry of Primitive Basalts: Evidence of an Anomalously Hot Mantle Source for Large Igneous Provinces. *Chemical Geology* 368: 1–10.

Delaney, J. S., Nehru, C. E., Prinz, M., and Harlow, G. E. 1981. Metamorphism in Mesosiderites. 12th Lunar and Planetary Science Conference, pp. 1315–42.

El Goresy, A., Zinner, E., Pellas, P., and Caillet, C. 2005. A Menagerie of Graphite Morphologies in the Acapulco Meteorite with Diverse Carbon and Nitrogen Isotopic Signatures: Implications for the Evolution History of Acapulcoite Meteorites. *Geochimica et Cosmochimica Acta* 69: 4535–56.

Faure, F., Trolliard, G., Nicollet, C., and Montel, J. M. 2003. A Developmental Model of Olivine Morphology as a Function of the Cooling Rate and the Degree of Undercooling. *Contributions to Mineralogy and Petrology* 145: 251–63.

Floran, R. J. 1978. Silicate Petrography, Classification, and Origin of the Mesosiderites: Review and New Observations. 9th Lunar and Planetary Science Conference, pp. 1053–81.

Floran, R. J., Caulfield, J. B. D., Harlow, G. E., Prinz, M. 1978. Impact-Melt Origin for the Simondium, Pinnaroo, and Hainholz Mesosiderites: Implications for Impact Processes Beyond the Earth-Moon System. 9th Lunar and Planetary Science Conference, pp. 1083–114.

Fuchs, L. H. 1969. The Phosphate Mineralogy of Meteorites. In *Meteorite Research*, edited by P. M. Millman, 683–95. Dordrecht: D. Reidel.

Ganguly, J., Yang, H., and Ghose, S. 1994. Thermal History of Mesosiderites: Quantitative Constraints from Compositional Zoning and Fe-Mg Ordering in Orthopyroxenes. *Geochimica et Cosmochimica Acta* 58: 2711–23.

Gardner-Vandy, K. G., Hill, D. H., Lauretta, D. S., Goreva, Y. S., Domanik, K. J., Greenwood, R. C., Franchi, I. A., and Killgore, M. 2011. Petrology and Geochemistry of the Northwest Africa 3368 Eucrite. *Meteoritics & Planetary Science* 46: 1052–70.

Ghiorso, M. S., and Gualda, G. A. R. 2015. An H_2O-CO_2 Mixed Fluid Saturation Model Compatible with Rhyolite-MELTS. *Contributions to Mineralogy and Petrology* 169: 1–30.

Goodrich, C. A., and Delaney, J. S. 2000. Fe/Mg–Fe/Mn Relations of Meteorites and Primary Heterogeneity of Primitive Achondrite Parent Bodies. *Geochimica et Cosmochimica Acta* 64: 149–60.

Goodrich, C. A., Kita, N. T., Spicuzza, M. J., Valley, J. W., Zipfel, J., Mikouchi, T., and Miyamoto, M. 2011. The Northwest Africa 1500 Meteorite: Not a Ureilite, Maybe a Brachinite. *Meteoritics & Planetary Science* 45: 1906–28.

Goodrich, C. A., Kita, N. T., Sutton, S. R., Wirick, S., and Gross, J. 2017. The Miller Range 090340 and 090206 Meteorites: Identification of New Brachinite-Like Achondrites with Implications for the Diversity and Petrogenesis of the Brachinite Clan. *Meteoritics & Planetary Science* 52: 949–78.

Greenwood, R. C., Barrat, J. A., Scott, E. R. D., Haack, H., Buchanan, P. C., Franchi, I. A., Yamaguchi, A., Johnson, D., Bevan, A. W. R., and Burbine, T. H. 2015. Geochemistry and Oxygen Isotope Composition of Main-Group Pallasites and Olivine-Rich Clasts in Mesosiderites: Implications for the "Great Dunite Shortage" and HED-Mesosiderite Connection. *Geochimica et Cosmochimica Acta* 169: 115–36.

Greenwood, R. C., Franchi, I. A., Jambon, A., Barrat, J. A., and Burbine, T. H. 2006. Oxygen Isotope Variation in Stony-Iron Meteorites. *Science* 313: 1763–5.

Gualda, G. A. R., Ghiorso, M. S., Lemons, R. V., and Carley, T. L. 2012. Rhyolite-MELTS: A Modified Calibration of MELTS Optimized for Silica-Rich, Fluid-Bearing Magmatic Systems. *Journal of Petrology* 53: 875–90.

Haack, H., Scott, E. R. D., and Rasmussen, K. L. 1996. Thermal and Shock History of Mesosiderites and their Large Parent Asteroid. *Geochimica et Cosmochimica Acta* 60: 2609–19.

Haba, M. K., Wotzlaw, J. F., Lai, Y. J., Yamaguchi, A., and Schönbächler, M. 2019. Mesosiderite Formation on Asteroid 4 Vesta by a Hit-and-Run Collision. *Nature Geoscience* 12: 510–5.

Haba, M. K., Yamaguchi, A., Kagi, H., Nagao, K., and Hidaka, H. 2017. Trace Element Composition and U-Pb Age of Zircons from Estherville: Constraints on the Timing of the Metal-Silicate Mixing Event on the Mesosiderite Parent Body. *Geochimica et Cosmochimica Acta* 215: 76–91.

Hahn, T. M., Jr., Lunning, N. G., McSween, H. Y., Jr., Bodnar, R. J., and Taylor, L. A. 2017. Dacite Formation on Vesta: Partial Melting of the Eucritic Crust. *Meteoritics & Planetary Science* 52: 1173–96.

Harlow, G. E., Delaney, J. S., Nehru, C. E., and Prinz, M. 1982. Metamorphic Reactions in Mesosiderites: Origin of Abundant Phosphate and Silica. *Geochimica et Cosmochimica Acta* 46: 339–48.

Hassanzadeh, J., Rubin, A. E., and Wasson, J. T. 1990. Compositions of Large Metal Nodules in Mesosiderites: Links to Iron Meteorite Group IIIAB and the Origin of Mesosiderite Subgroups. *Geochimica et Cosmochimica Acta* 54: 3197–208.

Hewins, R. H. 1979. The Pyroxene Chemistry of Four Mesosiderites. 10th Lunar and Planetary Science Conference, pp. 1109–25.

Hewins, R. H. 1984. The Case for a Melt Matrix in Plagioclase—POIK Mesosiderites. *Journal of Geophysical Research: Solid Earth* 89: C289–97.

Hopfe, W. D., and Goldstein, J. I. 2001. The Metallographic Cooling Rate Method Revised: Application to Iron Meteorites and Mesosiderites. *Meteoritics & Planetary Science* 36: 135–54.

Hrstka, T., Gottlieb, P., Skala, R., Breiter, K., and Motl, D. 2018. Automated Mineralogy and Petrology-Applications of TESCAN Integrated Mineral Analyzer (TIMA). *Journal of Geosciences* 63: 47–63.

Irving, A. J., Kuehner, S. M., and Ziegler, K. 2013. Petrology and Oxygen Isotopic Composition of Brachinite-like Achondrites Northwest Africa 7388 and Northwest Africa 7605, and Evidence for Late-Stage Methane-Triggered Reduction. 44th Lunar and Planetary Science Conference, abstract #2192.

Ishii, T., and Takeda, H. 1974. Inversion, Decomposition and Exsolution Phenomena of Terrestrial and Extraterrestrial Pigeonites. *Memoirs of Geological Society of Japan* 11: 19–36.

Jourdan, F., Forman, L., Kennedy, T., Benedix, G. K., Eroglu, E., and Mayers, C. 2021. End of Magmatism in the Upper Crust of Asteroid 4 Vesta. *Meteoritics & Planetary Science* 56: 619–41.

Kennedy, T., Jourdan, F., Eroglu, E., and Mayers, C. 2019. Bombardment History of Asteroid 4 Vesta Recorded by Brecciated Eucrites: Large Impact Event Clusters at 4.50 Ga and Discreet Bombardment Until 3.47 Ga. *Geochimica et Cosmochimica Acta* 260: 99–123.

Kimura, M., Ikeda, Y., Ebihara, M., and Prinz, M. 1991. New Enclaves in the Vaca Muerta Mesosiderite: Petrogenesis and Comparison with HED Meteorites. *Antarctic Meteorite Research* 4: 263–306.

Kimura, M., Sugiura, N., Yamaguchi, A., and Ichimura, K. 2020. The Most Primitive Mesosiderite Northwest Africa 1878, Subgroup 0. *Meteoritics & Planetary Science* 55: 1116–27.

Klein, C., and Dutrow, B. 2007. *Mineral Science*. Hoboken, NJ: John Wiley and Sons Inc. 675.

Kong, P., Su, W., Li, X. H., Spettel, B., Palme, H., and Tao, K. J. 2008. Geochemistry and Origin of Metal, Olivine Clasts, and Matrix in the Dong Ujimqin Qi Mesosiderite. *Meteoritics & Planetary Science* 43: 451–60.

Kring, D. A., and Cohen, B. A. 2002. Cataclysmic Bombardment Throughout the Inner Solar System 3.9–4.0 Ga. *Journal of Geophysical Research: Planets* 107: 4-1–4-6.

Krot, A. N., Keil, K., Scott, E. R. D., Goodrich, C. A., and Weisberg, M. K. 2014. Classification of Meteorites and Their Genetic Relationships. In *Treatise on Geochemistry*, edited by H. D. Holland and K. K. Turekian, 2nd ed., 1–137. Oxford: Elsevier Science.

Kullerud G., and Yoder H. S. Jr. 1963. *Sulfide-Silicate Reactions*. Washington, DC: Carnegie Institution of Washington Yearbook.

Langendam, A. D., Tomkins, A. G., Evans, K. A., Wilson, N. C., MacRae, C. M., Stephen, N. R., and Torpy, A. 2021. CHOS Gas/Fluid-Induced Reduction in Ureilites. *Meteoritics & Planetary Science* 56: 2062–82.

Lelarge, S. I., Folco, L., Masotta, M., Greenwood, R. C., Russell, S. S., and Bates, H. C. 2022. Asteroids Accretion, Differentiation, and Break-Up in the Vesta Source Region: Evidence from Cosmochemistry of Mesosiderites. *Geochimica et Cosmochimica Acta* 329: 135–51.

Li, S. J., Leya, I., Wang, S. J., Thomas, S., Bao, H. M., Fan, Y., and Mo, B. 2021. Exposure History, Petrology, and Shock-Induced Sulfidization Reaction of Alatage Mountain 001 Strewn Field Samples. *Meteoritics & Planetary Science* 56: 1293–310.

Liao, S. Y., and Hsu, W. B. 2017. The Petrology and Chronology of NWA 8009 Impact Melt Breccia: Implication for Early Thermal and Impact Histories of Vesta. *Geochimica et Cosmochimica Acta* 204: 159–78.

Lindstrom, M. M., and Salpas, P. A. 1983. Geochemical Studies of Feldspathic Fragmental Breccias and the Nature of North Ray Crater Ejecta. *Journal of Geophysical Research* 88: A671–83.

Lorenz, C. A., Nazarov, M. A., Brandstaetter, F., and Ntaflos, T. 2010. Metasomatic Alterations of Olivine Inclusions in the Budulan Mesosiderite. *Petrology* 18: 461–70.

Mayne, R. G., McSween, H. Y., Jr., McCoy, T. J., and Gale, A. 2009. Petrology of the Unbrecciated Eucrites. *Geochimica et Cosmochimica Acta* 73: 794–819.

McCall, G. J. H. 1966. The Petrology of the Mount Padbury Mesosiderite and Its Achondrite Enclaves. *Mineralogical Magazine and Journal of the Mineralogical Society* 36: 1029–60.

McCord, T. B., Adams, J. B., and Johnson, T. V. 1970. Asteroid Vesta: Spectral Reflectivity and Compositional Implications. *Science* 168: 1445–7.

McSween, H. Y., Jr., and Binzel, R. P. 2022. Protoplanet Vesta and HED Meteorites. In *Vesta and Ceres*, edited by S. Marchi, C. A. Raymond, and C. T. Russell, 1st ed., 41–52. Cambridge: Cambridge University Press.

McSween, H. Y., Jr., Binzel, R. P., DeSanctis, M. C., Ammannito, E., Prettyman, T. H., Beck, A. W., Reddy, V., et al., 2013. Dawn; the Vesta–HED Connection; and the Geologic Context for Eucrites, Diogenites, and Howardites. *Meteoritics & Planetary Science* 48: 2090–104.

Metzler, K., Bobe, K. D., Palme, H., Spettel, B., and Stöffler, D. 1995. Thermal and Impact Metamorphism on the HED Parent Asteroid. *Planetary and Space Science* 43: 499–525.

Mikouchi, T., Koizumi, E., Monkawa, A., Ueda, Y., and Miyamoto, M. 2003. Mineralogy and Petrology of Yamato 000593: Comparison with Other Martian Nakhlite Meteorites. *Antarctic Meteorite Research* 16: 34–57.

Mittlefehldt, D. W. 1990. Petrogenesis of Mesosiderites: I. Origin of Mafic Lithologies and Comparison with Basaltic Achondrites. *Geochimica et Cosmochimica Acta* 54: 1165–73.

Mittlefehldt, D. W. 2005. Ibitira: A Basaltic Achondrite from a Distinct Parent Asteroid and Implications for the Dawn Mission. *Meteoritics & Planetary Science* 40: 665–77.

Mittlefehldt, D. W. 2014. Achondrites. In *Treatise on Geochemistry*, edited by H. D. Holland and K. K. Turekian, 2nd ed., 235–66. Oxford: Elsevier Science.

Mittlefehldt, D. W. 2015. Asteroid (4) Vesta: I. the Howardite-Eucrite-Diogenite (HED) Clan of Meteorites. *Geochemistry* 75: 155–83.

Mittlefehldt, D. W., Greenwood, R. C., Berger, E. L., Loan, L. E., Peng, Z. X., and Ross, D. K. 2021. Eucrite-Type

Achondrites: Petrology and Oxygen Isotope Compositions. *Meteoritics & Planetary Science* 57: 484–526.

Mittlefehldt, D. W., McCoy, T. J., Goodrich, C. A., and Kracher, A. 1998. Non-Chondritic Meteorites from Asteroidal Bodies. In *Planetary Materials*, edited by J. J. Papike, vol. 36, 4-1–4-195. Washington, DC: Mineralogical Society of America.

Mittlefehldt, D. W., Prettyman, T. H., Reedy, R. C., Beck, A. W., Blewett, D. T., Gaffey, M. J., Lawrence, D. J., et al. 2012. Do Mesosiderites Reside on 4 Vesta? An Assessment Based on Dawn GRaND Data. 43rd Lunar and Planetary Science Conference, abstract #1655.

Miyamoto, M., Mikouchi, T., and Kaneda, K. 2001. Thermal History of the Ibitira Noncumulate Eucrite as Inferred from Pyroxene Exsolution Lamella: Evidence for Reheating and Rapid Cooling. *Meteoritics & Planetary Science* 36: 231–7.

Miyamoto, M., and Takeda, H. 1977. Evaluation of a Crust Model of Eucrites from the Width of Exsolved Pyroxene. *Geochemical Journal* 11: 161–9.

Müller, W. F. 1993. Thermal and Deformation History of the Shergotty Meteorite Deduced from Clinopyroxene Microstructure. *Geochimica et Cosmochimica Acta* 57: 4311–22.

Nakamuta, Y., Urata, K., Shibata, Y., and Kuwahara, Y. 2017. Effect of $NaCrSi_2O_6$ Component on Lindsley's Pyroxene Thermometer: An Evaluation Based on Strongly Metamorphosed LL Chondrites. *Meteoritics & Planetary Science* 52: 511–21.

Nehru, C. E., Harlow, G. E., Prinz, M., and Hewins, R. H. 1978. The Tridymite-Phosphate-Rich Component in Mesosiderites. *Meteoritics* 13: 573.

Norman, M. D. 1981. Petrology of Suevitic Lunar Breccia 67016. 12th Lunar and Planetary Science Conference, pp. 235–52.

Papike, J. J., Karner, J. M., and Shearer, C. K. 2003. Determination of Planetary Basalt Parentage: A Simple Technique Using the Electron Microprobe. *American Mineralogist* 88: 469–72.

Patzer, A., Hill, D. H., and Boynton, W. V. 2003. New Eucrite Dar al Gani 872: Petrography, Chemical Composition, and Evolution. *Meteoritics & Planetary Science* 38: 783–94.

Patzer, A., and McSween, H. Y., Jr. 2012. Ordinary (Mesostasis) and Not-So-Ordinary (Symplectites) Late-Stage Assemblages in Howardites. *Meteoritics & Planetary Science* 47: 1475–90. https://doi.org/10.1111/j.1945-5100.2012.01408.x

Petaev, M. I., and Brearley, A. J. 1994. Lamellar Olivine in the Divnoe Achondrite: EPMA and TEM Studies. 25th Lunar and Planetary Science Conference, abstract #1535.

Pittarello, L., McKibbin, S., Yamaguchi, A., Ji, G., Schryvers, D., Debaille, V., and Claey, P. 2019. Two Generations of Exsolution Lamellae in Pyroxene from Asuka 09545: Clues to the Thermal Evolution of Silicates in Mesosiderite. *American Mineralogist* 104: 1663–72.

Pouchou, J. L., and Pichoir, F. 1985. "PAP" (Phi-Rho-Z) Procedure for Improved Quantitative Microanalysis. In *Microbeam Analysis*, edited by J. T. Armstrong, 104–6. San Francisco, CA: San Francisco Press.

Powell, B. N. 1969. Petrology and Chemistry of Mesosiderites—I. Textures and Composition of Nickel-Iron. *Geochimica et Cosmochimica Acta* 33: 789–810.

Powell, B. N. 1971. Petrology and Chemistry of Mesosiderites—II. Silicate Textures and Compositions and Metal-Silicate Relationships. *Geochimica et Cosmochimica Acta* 35: 5–34.

Prettyman, T. H., Mittlefehldt, D. W., Yamashita, N., Lawrence, J. D., Beck, A. W., Feldman, W. C., McCoy, T. J., et al. 2012. Elemental Mapping by Dawn Reveals Exogenic H in Vesta's Regolith. *Science* 338: 242–6.

Putirka, K. D. 2008. Thermometers and Barometers for Volcanic Systems. *Reviews in Mineralogy and Geochemistry* 69: 61–120.

Rubin, A. E. 1997. A History of the Mesosiderite Asteroid: Enigmatic Meteorites, Mixtures of Iron and Stone, Can be Understood by Unraveling the Evolutionary History of their Parent Asteroid. *American Scientist* 85: 26–35.

Rubin, A. E., and Jerde, E. A. 1987. Diverse Eucritic Pebbles in the Vaca Muerta Mesosiderite. *Earth and Planetary Science Letters* 84: 1–14.

Rubin, A. E., and Mittlefehldt, D. W. 1993. Evolutionary History of the Mesosiderite Asteroid: A Chronologic and Petrologic Synthesis. *Icarus* 101: 201–12.

Rumble, D. III, Irving, A. J., Bunch, T. E., Wittke, J. H., and Kuehner, S. M. 2008. Oxygen Isotopic and Petrological Diversity Among Brachinites NWA 4872, NWA 4874, NWA 4882 and NWA 4969: How Many Ancient Parent Bodies? 39th Lunar and Planetary Science Conference, abstract #1974.

Ruzicka, A., Boynton, W. V., and Ganguly, J. 1994. Olivine Coronas, Metamorphism, and the Thermal History of the Morristown and Emery Mesosiderites. *Geochimica et Cosmochimica Acta* 58: 2725–41.

Schwartz, J. M., and McCallum, I. S. 2005. Comparative Study of Equilibrated and Unequilibrated Eucrites: Subsolidus Thermal Histories of Haraiya and Pasamonte. *American Mineralogist* 90: 1871–86.

Scott, E. R. D., Haack, H., and Love, S. G. 2001. Formation of Mesosiderites by Fragmentation and Reaccretion of a Large Differentiated Asteroid. *Meteoritics & Planetary Science* 36: 869–81.

Shearer, C. K., Burger, P., and Papike, J. J. 2010. Petrogenetic Relationships between Diogenites and Olivine Diogenites: Implications for Magmatism on the HED Parent Body. *Geochimica et Cosmochimica Acta* 74: 4865–80.

Stewart, B. W., Papanastassiou, D. A., and Wasserburg, G. J. 1994. Sm-Nd Chronology and Petrogenesis of Mesosiderites. *Geochimica et Cosmochimica Acta* 58: 3487–509.

Sugiura, K., Haba, M. K., and Genda, H. 2022. Giant Impact onto a Vesta-Like Asteroid and Formation of Mesosiderites Through Mixing of Metallic Core and Surface Crust. *Icarus* 379: 114949.

Sugiura, N., Arai, T., and Matsui, T. 2019. Northwest Africa 4747, an Unique Mesosiderite. 82nd Annual Meeting of The Meteoritical Society 82(2157). p. 6083.

Sugiura, N., and Kimura, M. 2015. Reheating and Cooling of Mesosiderites. 46th Lunar and Planetary Science Conference, abstract #1646.

Takeda, H., and Graham, A. L. 1991. Degree of Equilibration of Eucritic Pyroxenes and Thermal Metamorphism of the Earliest Planetary Crust. *Meteoritics* 26: 129–34.

Takeda, H., and Mori, H. 1985. The Diogenite-Eucrite Links and the Crystallization History of a Crust of Their Parent Body. *Journal of Geophysical Research: Solid Earth* 90: C636–48.

Tamaki, M., Yamaguchi, A., Misawa, K., Ebihara, M., and Takeda, H. 2006. Petrology and Geochemistry of a Silicate

Clast from the Mount Padbury Mesosiderite: Implications for Metal-Silicate Mixing Events of Mesosiderite. *Meteoritics & Planetary Science* 41: 1919–28.

Taylor, W. R. 1998. An Experimental Test of Some Geothermometer and Geobarometer Formulations for Upper Mantle Peridotites with Application to the Thermobarometry of Fertile Lherzolites and Garnet Websterite. *Neues Jahrbuch für Mineralogie-Abhandlungen* 172: 381–408.

Vaci, Z., Day, J. M. D., Paquet, M., Ziegler, K., Yin, Q. Z., Dey, S., Miller, A., Agee, C., Bartoschewitz, R., and Pack, A. 2021. Olivine-Rich Achondrites from Vesta and the Missing Mantle Problem. *Nature Communications* 12: 1–8.

Vernazza, P., Brunetto, R., Binzel, R. P., Perron, C., Fulvio, D., Strazzulla, G., and Fulchignoni, M. 2009. Plausible Parent Bodies for Enstatite Chondrites and Mesosiderites: Implications for Lutetia's Fly-by. *Icarus* 202: 477–86.

Viikinkoski, M., Vernazza, P., Hanuš, J., Coroller, H. L., Tazhenova, K., Carry, B., Marsset, M., et al. 2018. (16) Psyche: A Mesosiderite-Like Asteroid? *Astronomy & Astrophysics* 619: L3. https://doi.org/10.1051/0004-6361/201834091

Wadhwa, M., Shukolyukov, A., Davis, A. M., Lugmair, G. W., and Mittlefehldt, D. W. 2003. Differentiation History of the Mesosiderite Parent Body: Constraints from Trace Elements and Manganese-Chromium Isotope Systematics in Vaca Muerta Silicate Clasts. *Geochimica et Cosmochimica Acta* 67: 5047–69.

Wang, L. Y., Hsu, W. B., and Ma, C. Q. 2010. Petrology, Mineralogy and Geochemisty of Antarctic Mesosiderite GRV 020175: Implications for Its Complex Formation History. *Acta Geologica Sinica (English Edition)* 84: 528–42.

Wasson, J. T. 1999. Trapped Melt in IIIAB Irons: Solid/Liquid Elemental Partitioning During the Fractionation of the IIIAB Magma. *Geochimica et Cosmochimica Acta* 63: 2875–89.

Wasson, J. T., Choi, B. G., Jerde, E. A., and Ulff-Møller, F. 1998. Chemical Classification of Iron Meteorites: XII. New Members of the Magmatic Groups. *Geochimica et Cosmochimica Acta* 62: 715–24.

Wasson, J. T., Schaudy, R., Bild, R. W., and Chou, C. L. 1974. Mesosiderites—I. Compositions of their Metallic Portions and Possible Relationship to Other Metal-Rich Meteorite Groups. *Geochimica et Cosmochimica Acta* 38: 135–49.

Wells, P. R. A. 1977. Pyroxene Thermometry in Simple and Complex Systems. *Contributions to Mineralogy and Petrology* 62: 129–39.

Whitney, D. L., and Evans, B. W. 2010. Abbreviations for Names of Rock-Forming Minerals. *American Mineralogist* 95: 185–7.

Williams, H. M., Markowski, A., Quitté, G., Halliday, A. N., Teutsch, N., and Levasseur, S. 2006. Fe Isotope Fractionation in Iron Meteorites: New Insights into Metal-Sulphide Segregation and Planetary Accretion. *Earth and Planetary Science Letters* 250: 486–500.

Yamaguchi, A., Barrat, J. A., Greenwood, R. C., Shirai, N., Okamoto, C., Setoyanagi, T., Ebihara, M., Franchi, I. A., and Bohn, M. 2009. Crustal Partial Melting on Vesta: Evidence from Highly Metamorphosed Eucrites. *Geochimica et Cosmochimica Acta* 73: 7162–82.

Yamaguchi, A., Clayton, R. N., Mayeda, T. K., Ebihara, M., Oura, Y., Miura, Y. N., Haramura, H., Misawa, K., Kojima, H., and Nagao, K. 2002. A New Source of Basaltic Meteorites Inferred from Northwest Africa 011. *Science* 296: 334–6.

Yamaguchi, A., Taylor, G. J., and Keil, K. 1996. Global Crustal Metamorphism of the Eucrite Parent Body. *Icarus* 124: 97–112.

Yang, C. W., Williams, D. B., and Goldstein, J. I. 1997. A New Empirical Cooling Rate Indicator for Meteorites Based on the Size of the Cloudy Zone of the Metallic Phases. *Meteoritics & Planetary Science* 32: 423–9.

Zhang, A. C., Bu, Y. F., Pang, R. L., Sakamoto, N., Yurimoto, H., Chen, L. H., Gao, J. F., Du, D. H., Wang, X. L., and Wang, R. C. 2018. Origin and Implications of Troilite-Orthopyroxene Intergrowths in the Brecciated Diogenite Northwest Africa 7183. *Geochimica et Cosmochimica Acta* 220: 125–45.

Zhang, A. C., Kawasaki, N., Bao, H., Liu, J., Qin, L., Kuroda, M., Gao, J. F., et al. 2020. Evidence of Metasomatism in the Interior of Vesta. *Nature Communications* 11: 1289.

SUPPORTING INFORMATION

Additional supporting information may be found in the online version of this article.

Figure S1. (a) Mosaic BSE image of mesosiderite NWA 12949 whole-rock, contrast enhanced. (b) Mineral distributions of mesosiderite NWA 12949 whole-rock. The positions of five lithic clasts (Clasts I–V) referred to in the main text are labeled in red rectangles with respective names.

Figure S2. Distributions of ultramafic clasts and mafic to intermediate clasts in mesosiderite NWA 12949 whole-rock.

Figure S3. (a) BSE image of Clast V in NWA 12949. (b) Enlarged view of the red box in (a), indicating blurred and discontinuous relict lamellae in pyroxene of Clast V.

Table S1. Representative EPMA compositions of olivine in NWA 12949.

Table S2. Representative EPMA compositions of orthopyroxene in NWA 12949.

Table S3. Representative EPMA compositions of clinopyroxene in NWA 12949.

Table S4. Representative EPMA compositions of plagioclase in NWA 12949.

Table S5. Representative EPMA compositions of tridymite in NWA 12949.

Table S6. Representative EPMA compositions of chromite in NWA 12949.

Table S7. Representative EPMA compositions of Fe-Ti oxides in NWA 12949.

Table S8. Representative EPMA compositions of merrillite in NWA 12949.

Table S9. Representative EPMA compositions of mesostasis in NWA 12949.

Table S10. Bulk compositions of lithic clasts in NWA 12949.